Biomedicine & Pharmacotherapy 197 (2026) 119185

Contents lists available at ScienceDirect

Biomedicine & Pharmacotherapy

journal homepage: www.elsevier.com/locate/biopha

Synthesis and characterization of new P2X7 receptor antagonists as antitumor agents

Marianna Grignolo [a,1], Andrea Spinaci [b,1], Ludovica Ricci [a], Anna Pegoraro [a], Luigia Ruo [a], Catia Lambertucci [b], Daniele Vitone [c], Marcello Leopoldo [c], Enza Lacivita [c], Federica Fortuna [a], Michela Buccioni [b], Beatrice Francucci [b], Gabriella Marucci [b], Diego Dal Ben [b], Rosaria Volpini [b,1], Elena Adinolfi [a,*,1]

[a] Department of Medical Sciences, Section of Experimental Medicine, University of Ferrara, Via Luigi Borsari, 46, 44121, Italy
[b] School of Pharmacy, Medicinal Chemistry Unit, University of Camerino, Via Madonna delle Carceri snc, Camerino 62032, Italy
[c] Department of Pharmacy, Drug Science, University of Bari Aldo Moro, Via Orabona 4, Bari 70125, Italy

ARTICLE INFO

Keywords:
P2X7
Antagonists
Triazole
Benzamidine
Melanoma
Colon carcinoma
Glioblastoma
Tumor microenvironment
Extracellular vesicles

ABSTRACT

Extracellular ATP is a key component of the tumor microenvironment, where it promotes cancer progression by activating the P2X7 receptor (P2X7R). Prolonged receptor stimulation triggers the release of pro-tumorigenic extracellular vesicles and soluble factors, including IL-1β, VEGF, and TGFβ. Here, we report the design and characterization of novel triazole- and benzamide-based negative allosteric modulators of P2X7R. Among these, compounds **5** and **9** showed nanomolar affinity for the human receptor (K_i = 80 nM and 3.17 nM, respectively) and effectively inhibited calcium influx (IC_{50} 370 nM and 47 nM, respectively). Molecular docking supported distinct binding modes for the two scaffolds, aligning them with known allosteric inhibitors through interactions with Lys297, Asp92, and hydrophobic subpockets. Compounds **5** and **9** displayed favorable metabolic stability in mouse liver microsomes and efficiently blocked P2X7R-dependent signaling in melanoma, glioblastoma, and colon carcinoma cells. Treatment with both compounds significantly reduced tumor cell proliferation, invasiveness, and extracellular vesicle release, with efficacy comparable to or greater than that of the reference antagonist A740003. In vivo, both molecules suppressed melanoma growth in syngeneic mice and modulated cytokine levels in the TME by increasing IFN-γ while reducing VEGF, IL-1β, and TGF-β. These findings identify compounds **5** and **9** as potent, selective, and metabolically stable P2X7R antagonists with translational potential as anticancer agents targeting both tumor growth and extracellular vesicle-mediated communication.

1. Introduction

1.1. Biological background and pathological significance

Extracellular ATP (eATP) is a critical component of the tumour microenvironment (TME), released through various mechanisms, including necrosis at the core of expanding tumors. These elevated eATP levels are consistent with the activation of the P2X7 receptor (P2X7R), an ATP-gated ion channel highly expressed on both immune and tumour cells. Upon transient stimulation, P2X7R facilitates the cellular influx of Na^+ and Ca^{2+}, and the efflux of K^+; however, prolonged exposure to high ATP concentrations induces a conformational change that forms a non-selective macropore associated with cell death [1]. Structurally, the receptor is a trimer, and each monomer comprises two transmembrane α-helices, distinct cytoplasmic N- and extended C-terminal domains, and a large extracellular loop critical for ligand binding [2], which is targeted by the potent synthetic agonist 2′(3′)-O-(4-benzoylbenzoyl) ATP (BzATP) [3]. Furthermore, crystallographic studies have revealed a

* Corresponding author.
E-mail addresses: marianna.grignolo@unife.it (M. Grignolo), andrea.spinaci@unicam.it (A. Spinaci), ludovica.ricci@unife.it (L. Ricci), anna.pegoraro@unife.it (A. Pegoraro), luigia.ruo@unife.it (L. Ruo), catia.lambertucci@unicam.it (C. Lambertucci), daniele.vitone@uniba.it (D. Vitone), marcello.leopoldo@uniba.it (M. Leopoldo), enza.lacivita@uniba.it (E. Lacivita), federica.fortuna@unife.it (F. Fortuna), michela.buccioni@unicam.it (M. Buccioni), beatrice.francucci@unicam.it (B. Francucci), gabriella.marucci@unicam.it (G. Marucci), diego.dalben@unicam.it (D.D. Ben), rosaria.volpini@unicam.it (R. Volpini), elena.adinolfi@unife.it (E. Adinolfi).
[1] These authors equally contributed to the study.

https://doi.org/10.1016/j.biopha.2026.119185
Received 2 December 2025; Received in revised form 17 February 2026; Accepted 28 February 2026
Available online 11 March 2026

unique allosteric binding site for antagonists, highlighting potential targets for drug design [4,5]. Accumulating evidence indicates that P2X7R plays a central role in oncogenesis [6–10], promoting cancer cell proliferation [11–14], motility, and metastatic dissemination in multiple animal models [15–19]. P2X7 antagonism has been shown to reduce tumour burden and enhance sensitivity to radio and chemotherapy [13, 30,31]. Mechanistically, P2X7R associates with neovascularisation [11, 12,20], the activation of pro-tumorigenic signalling pathways [21,22], and oncogene mutations [23]. It also mediates the release of pro-tumoral extracellular vesicles [18,23] and modulates the immune landscape via NLRP3 inflammasome activation and cytokine secretion [23–26]. Consequently, P2X7R function is intrinsically linked to major alterations in tumor-associated immune responses, such as reported fluctuations in IFN-γ and TGF-β levels [20,27–29].

1.2. Pharmacological landscape

Despite the promising therapeutic potential of targeting P2X7R, clinical translation remains limited. While a monoclonal antibody targeting a specific non-macropore-forming isoform has been tested [32, 33], most findings rely on experimental models, underscoring the need to develop patentable small-molecule antagonists for inflammatory conditions and cancer [34]. Early preclinical tools such as periodate-oxidized ATP (oxo-ATP), brilliant blue G (BBG), and KN62 demonstrated efficacy [35–37] but lacked sufficient selectivity [38]. Conversely, newer compounds like A-740003, A-438079, AZ10606120, and the JNJ series act as selective and potent blockers of human and rodent P2X7R [13,39,40], alongside potential biologicals such as nanobodies [41]. Structurally, the most characterized inhibitors are non-competitive allosteric modulators (Fig. 1). These include cyanoguanidine derivatives (e.g., A-740003), which feature an aromatic group linked to a moiety with H-bond acceptor/donor functions and a hydrophobic terminal chain. This pharmacophoric profile is shared by quinoline derivatives and benzamides, such as the adamantane-containing compound AZ10606120 and its structural analogues, such as SMW64–16 [34]. Additionally, disubstituted azoles represent a key class of antagonists; evolving from initial tetrazole scaffolds (e.g., A-438079), recent optimization efforts have involved varying phenyl/benzyl substituents, incorporating di- or triazole rings, and modifying linkers to yield nanomolar-range inhibitors like A-839977 [34].

1.3. Study aims

Building upon these structural insights, here we identified novel triazole- and benzamide-based P2X7R antagonists with favorable pharmacological profiles. We modeled their docking at the human P2X7R and evaluated their capacity to reduce tumor growth, extracellular vesicle release, invasiveness, and pro-tumorigenic cytokine secretion, while enhancing anti-tumour immune responses *in vivo*. Collectively, our data support the further preclinical development of these compounds as P2X7R modulators for the treatment of aggressive and treatment-resistant cancers, including melanoma, glioblastoma, and colon carcinoma.

2. Results and discussion

2.1. Design and synthesis of new P2XR ligands

In a search for potent P2X7R negative allosteric modulators, an extensive literature study led us to identify two series of molecules with 1-(2,3-dichlorophenyl)-1*H*-1,2,4-triazole-5-ammino and 2-chloro-3-methoxybenzamido scaffolds of general formula reported in Fig. 2A. These compounds, analogues of the above reported inhibitors SMW64–16 and A839977, are described in two patent applications as potent P2X7R inhibitors endowed with nM activity in functional studies [42,43]. On these bases, we decided to introduce different substituents in the above-mentioned scaffolds at the amino/amido portions as reported in Fig. 2B. We chose the diphenylmethyl group as an analogue of heterocycloalky/arylmethyl chains present in many compounds

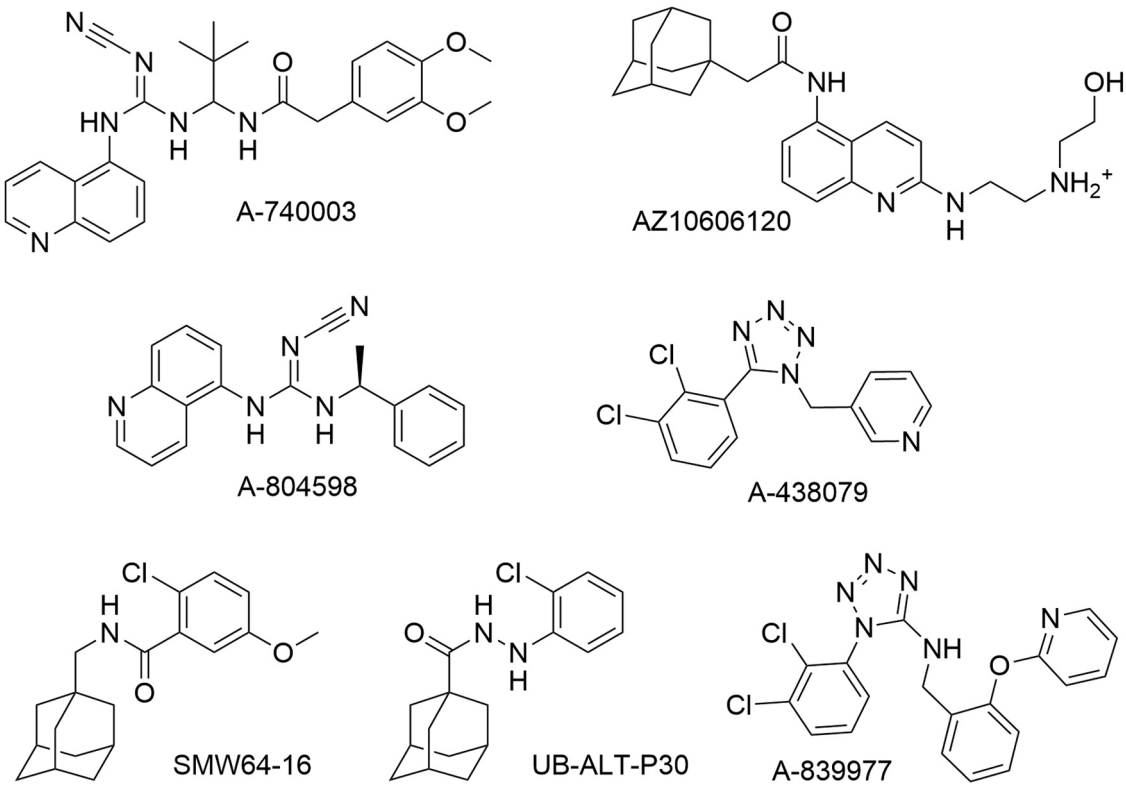

Fig. 1. Structures of known P2X7R allosteric inhibitors.

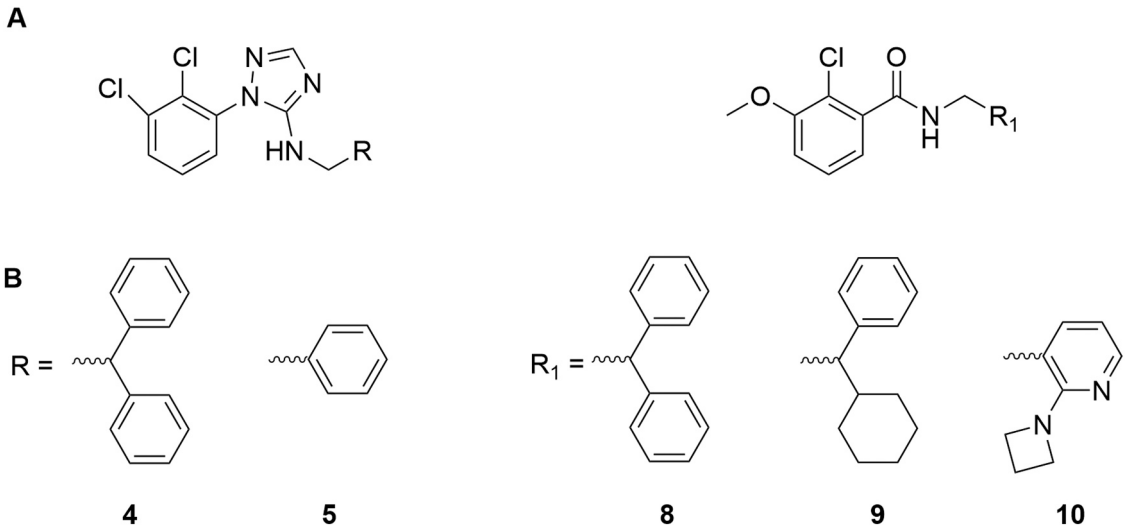

Fig. 2. (A) General structures of P2X7R modulators endowed with triazole-ammino and benzamido scaffolds; (B) structures of the substituents introduced in the selected scaffolds.

reported in one of the patents [42]. Then, we simplified this substituent with a single phenyl ring or replaced one or both phenyl rings with different cycles.

Compounds **4** and **5** were synthesized according to Florjancic et al. [44]. Hence, 2,3-dichlorophenylhydrazine hydrochloride (**1**) was reacted with formamide at 120 °C for 16 h to get the triazole derivative **2** with 79% yield. **2** was then selectively brominated in 5-position with N-bromosuccinimide (NBS) in the presence of benzoyl peroxide at 80 °C for 12 h. The obtained compound **3** was reacted with suitable commercial arylalkylamines to get the desired **4** and **5** with 4% and 20% yields, respectively (Scheme 1). According to the patent application [43], the 2-chloro-3-methoxybenzamido derivatives **8–10** were synthesized starting from commercial 2-chloro-3-methoxybenzaldehyde (**6**), which was oxidized with $KMnO_4$ in basic conditions at 90 °C for 5 h. The obtained acid **7** was then activated with 1-ethyl-3-(3-dimethylaminopropyl)carbodiimide (EDC) in the presence of hydroxybenzotriazole (HOBt) and *N*,*N*-diisopropylethylamine (DIPEA) at room temperature (r.t.) for 1 h, and the suitable amines were then added. From these reactions, the desired compounds **8–10** were obtained with yields ranging from 12% to 26% (Scheme 2). Among the used amines, the 2-cyclohexyl-2-phenylethylamine (**12**) was obtained by catalytic reduction of the commercial 2-cyclohexyl-2-phenylacetonitrile (**11**), while the [(2-(azetidin-1-yl)pyridin-3-yl]methanamine (**15**) was prepared by reduction of the corresponding nitrile **14**. 2-(Azetidin-1-yl) nicotinonitrile (**14**) was synthesized from commercial 2-fluoronicotinonitrile (**13**) by reaction with azetidine hydrochloride (Scheme 3).

2.2. Binding at hP2X7R

All the synthesized compounds were evaluated in binding studies at recombinant hP2X7R. HEK-293 cells have been widely used over time because they do not express any P2X receptor and can be efficiently transfected [45]. In our laboratory, we have developed HEK-293 cells stably expressing the recombinant hP2X7R at the cell membrane (Fig. 3, A), which we have utilized in several P2X7R-related assays, including binding, functional, proliferation, and cancer-related studies [11, 46–48]. First, we set up the experimental conditions for the binding assay using [^{3}H]-JNJ-64413739 as the radioligand to assess the compounds' affinity, expressed as the inhibition constant (Ki) (Fig. 3, B). Membrane preparations were obtained from the above-mentioned hP2X7R-expressing HEK-293 cells (Fig. 3,A), and the dissociation constant (K_D) of the P2X7R radioligand [^{3}H]-JNJ-64413739 was measured in saturation-binding experiments (Fig. 3, B). [^{3}H]JNJ-64413739 binds P2X7R with high affinity, as demonstrated by saturation assays, and in a concentration-dependent manner with saturable specific binding. The radiolabeled compound exhibited a K_D of 8.2 nM, and full saturation was observed at approximately 40 nM (Fig. 3 B). Results of binding studies are reported in (Fig. 3,B) as K_i (nM); cold JNJ-64413739 was tested as a reference compound. It showed a $K_i = 12$ nM, in agreement with that reported in the literature ($K_i = 15.9$) [69]. The presence of the steric hindered diphenyethyl at the 1-(2,3-dichlorophenyl)-1H-1,2,4-triazole-5-ammino scaffold gave a different result in comparison to the smaller benzyl substituent. In fact, **5**, bearing the benzyl group, showed a higher affinity than **4**, with K_is of 80 nM and 440 nM, respectively (Fig. 3,B). On the contrary, the presence of steric hindrance substituents at the 2-chloro-3-methoxybenzamido scaffold results in compounds endowed with high P2X7R affinity; the cyclohexyl derivative **9** (K_i = 3.17 nM) presents a two-fold higher affinity with respect to the diphenylethyl analogue **8** ($K_i = 7.30$ nM) (Fig. 3,B). On the other hand, when a 2-azetidinyl pyridinyl chain was introduced at the same scaffold, the affinity decreased, leading to compound **10** (K_i = 584 nM), which showed a comparable affinity to **4** (Fig. 3,B). These data demonstrate that the two scaffolds deeply influence binding affinity at hP2X7R, likely due to their different orientations within the receptor binding site. To

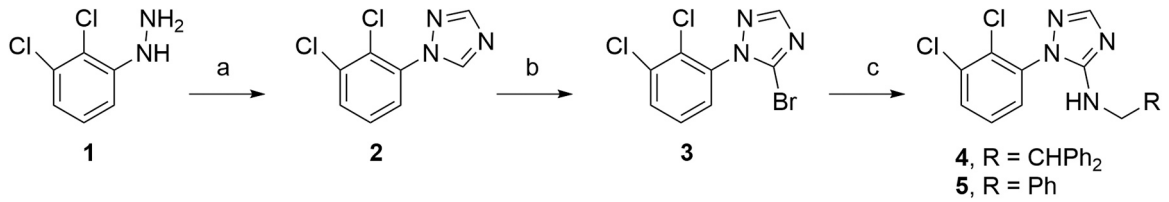

Scheme 1. Synthesis of compounds **4** and **5**. Reagents and conditions: a) formamide, 120 °C, 16 h; b) NBS, benzoyl peroxide, CCl_4, 80 °C, 12 h; c) arylalkylamine, 140 °C, 12 h.

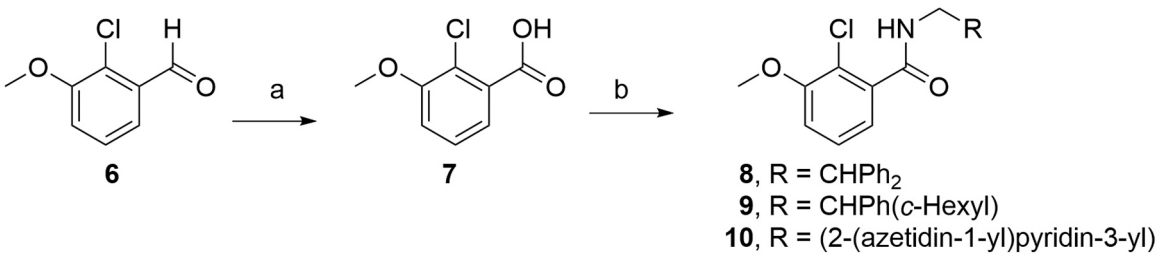

Scheme 2. Synthesis of compounds **8-10.** Reagents and conditions: a) $KMnO_4$, sol. $NaHCO_3$, 90 °C, 5 h; b) arylalkylamine, EDC, HOBt, DIPEA, r.t., 12 h.

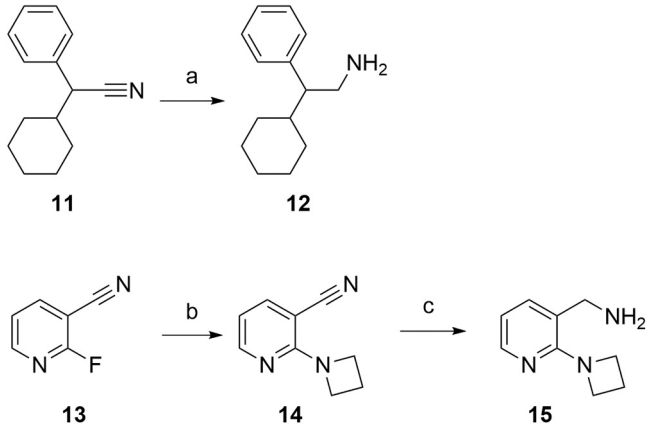

Scheme 3. Synthesis of amine intermediates **12** and **15**. Reagents and conditions: a) H_2 (60 psi), HCl, Pd/C, EtOH, r.t., 12 h; b) azetidine hydrochloride, Et_3N, THF, 60 °C, 16 h; c) H_2 (60 psi), NH_3 in MeOH, Ni Raney, 50 °C, 6 h.

verify this hypothesis, molecular modeling studies were conducted.

2.3. Molecular modeling studies

Molecular docking studies were performed to simulate the binding mode of the synthesised compounds at the hP2X7R. For this task, we employed the recently reported electron cryomicroscopy (cryo-EM) structure of the hP2X7R in complex with the allosteric inhibitor UB-ALT-P30 (Fig. 1; PDB code: 9E3O [49]). Molecular docking experiments were performed within MOE (Molecular Operating Environment) software suite interface [50]. MOE docking and scoring tools were employed, followed by energy minimization processes to optimize each ligand-target complex. The top-scoring conformations for each compound were selected for visualization and analysis.

Docking results for synthesised compounds **8-10** show the molecules placing their amide functions in the central region of the allosteric binding cavity of hP2X7R, making polar interactions with Lys297 and Asp92. The substituted benzoyl ring is placed almost in a corresponding position of the phenyl ring of the compound UB-ALT-P30 as observed from cryo-EM data (Fig. 4), while the aryl-alkyl group is placed toward the core of the receptor. Based on this conformation, compounds **8** and **9** present their arylalkyl group in an arrangement making a ring (phenyl and c-hexyl, respectively) being placed in a hydrophobic sub-pocket given by hP2X7R residues Phe103, Met105, Phe293, and Val312, while the other ring (a phenyl group in both compounds) being oriented toward the central region of the receptor and being surrounded by residues Phe95, Tyr295, and Tyr298 (Fig. 4).

Docking results for compounds **4** and **5** did not suggest a clear binding mode at the (cryo-EM) structure of the hP2X7R. This was probably greatly influenced by the orientation of Lys297 side chain, whose hindrance prevents **4** ad **5** to adopt a stable conformation in the cavity. Lys297 is observed to adopt various arrangements within the cavity, depending on the bound ligands, in previously reported

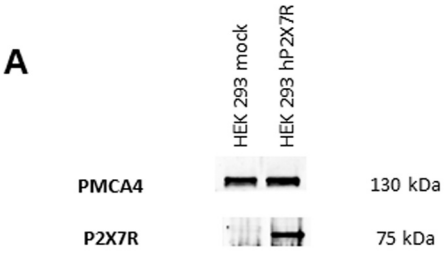

B

Comp	K_D (nM)[a]	K_i (nM)[b]
[^{3}H]-JNJ64413739	8.2 ± 1.1	
JNJ-64413739		12 ± 0.082
4		440 ± 80
5		80 ± 9
8		7.30 ± 1.7
9		3.17 ± 0.7
10		584 ± 60

Fig. 3. (A) Immunoblot showing P2X7R expression in cell membrane extracts from HEK 293 cells stably transfected with an empty vector (mock) or hP2X7. (B) [^{3}H]-JNJ64413739 K_D and compound K_i values in binding assays at hP2X7R transfected in HEK293 cells. [a]K_D was calculated from the binding saturation curve obtained at a radioligand concentration of 40 nM. [b]Displacement of specific [^{3}H]-JNJ64413739 binding. Data are expressed as means ± SE.

experimental structures of P2X7R [4,49,51]. For this reason, we decided to develop a hP2X7R homology model based on the 3D structure of the rat P2X7R obtained by electron cryomicroscopy (cryo-EM) in complex with A-839977 as a template (Fig. 1; PDB code: 8TR7, [51]). This choice was made due to the structural similarity of compounds **4-5** and compound A-839977 and to the consequent binding site arrangement in complex with this class of compounds. Docking results for this 3D model show that compounds **4–5** are oriented within the binding cavity in a manner very similar to that of A-839977, with the amine linker forming a polar interaction with Asp92 (Fig. 5).

The dichlorophenyl ring of **4** and **5** adopts an analogous position and orientation to the same group of A-839977, making similar interactions with the binding cavity (residues Phe103, Met105, Phe293, and Val312). The arylalkyl groups of **4** and **5** get positioned analogously to the benzyl ring of A-839977. In this case, the different sizes of the two groups lead to distinct interactions with the receptor cavity, with compound **4** showing slightly lower affinity than **5**, possibly due to

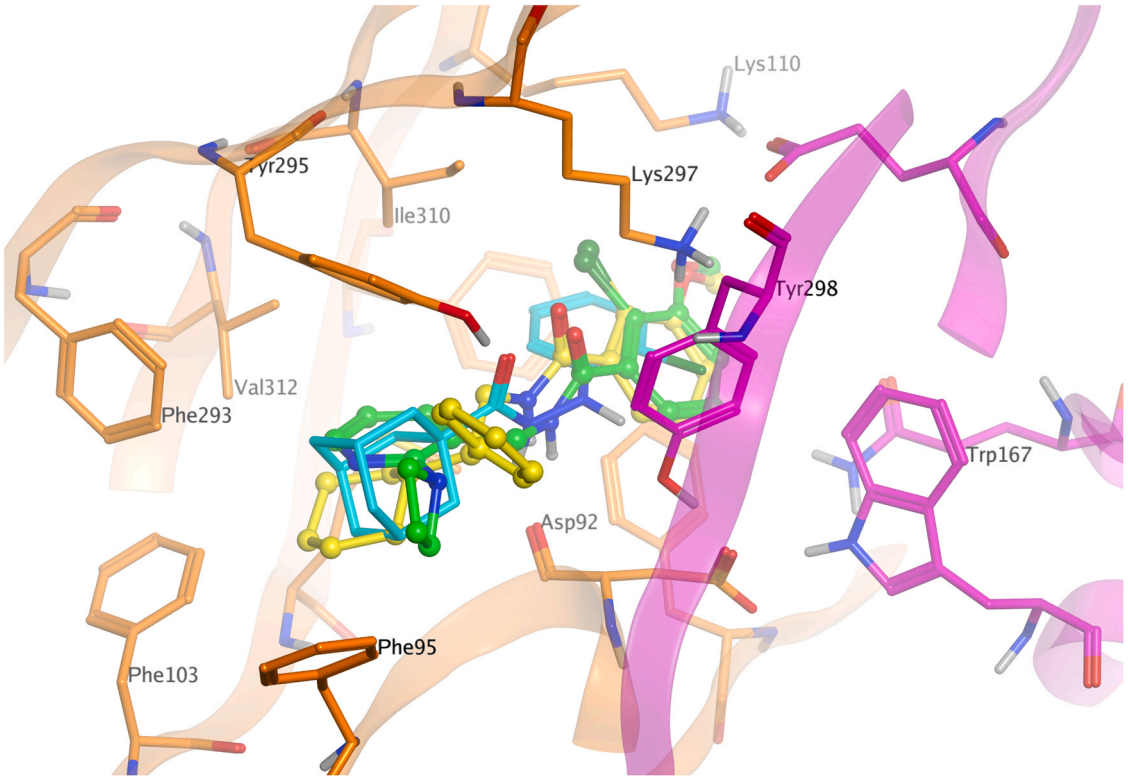

Fig. 4. Docking conformations of compounds **9** and **10** at the hP2X7 experimental structure (PDB code: 9E3O). Key residues for ligand-target interaction are indicated. Colour coding: compounds **9** and **10**, yellow and green, respectively; compound UB-ALT-P30 (complexed with the hP2X7 receptor in the 9E3O structure) is shown for comparison and coloured cyan. See text for description.

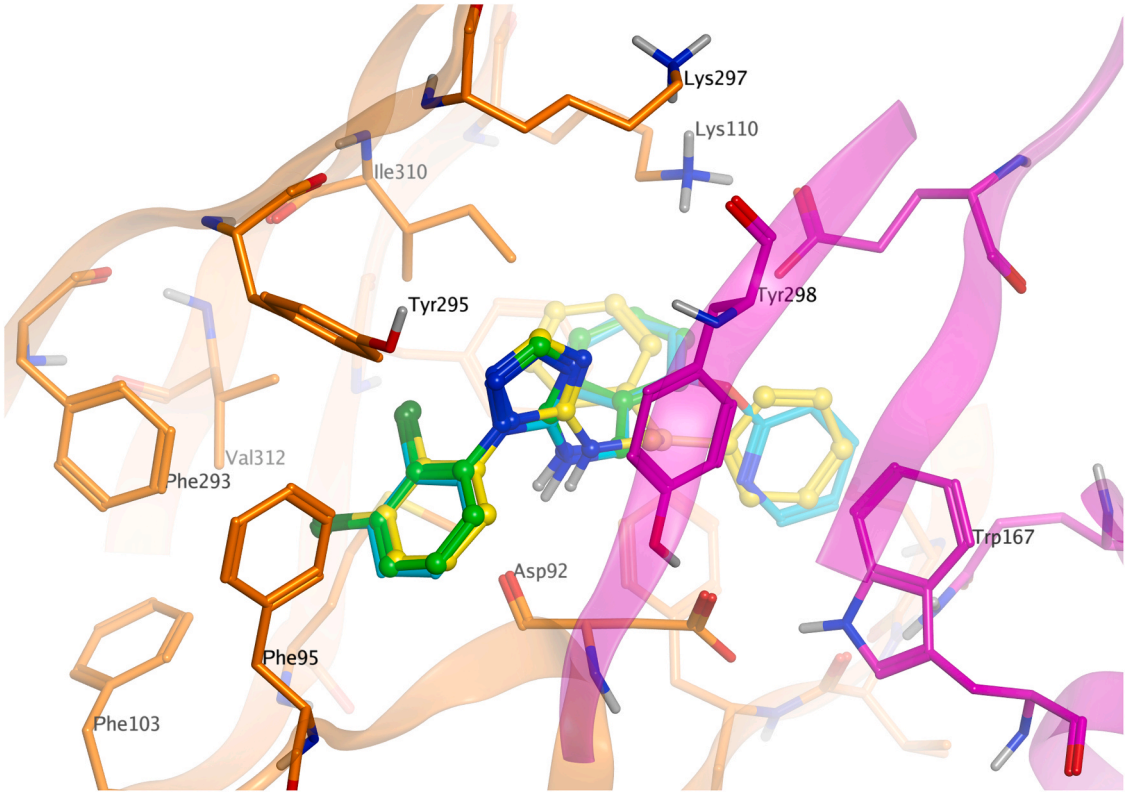

Fig. 5. Docking conformations of compounds **4** and **5** at the 8TR7-based hP2X7 homology model. Key residues for ligand-target interaction are indicated. Colour coding: compounds **4** and **5**, yellow and green, respectively; compound A-839977 (complexed with the rat P2X7 receptor in the 8TR7 structure) is shown for comparison and coloured cyan. See text for description.

hindrance from its arylalkyl substituent.

These results demonstrate that the orientation within the binding site and the consequent interaction with the receptor differ between the two sets of compounds, **8**-**10** and **4**-**5**. The same results also show that, within the same class of compounds, the steric and chemical-physical properties of substituents are associated with varying degrees of affinity for hP2X7R.

2.4. In vitro metabolic stability

Based on the binding studies results, compounds **5** and **9**, which exhibited the best affinity among the two mini-series, were selected for further biological characterization. Given that several P2X7R antagonists failed to demonstrate *in vivo* efficacy due to poor pharmacokinetic properties [34], we assessed their *in vitro* metabolic stability in mouse liver microsomes. Indeed, liver microsomes are a widely used system for evaluating a molecule's susceptibility to first-pass metabolism, the primary mechanism of *in vivo* metabolic degradation [52]. We also included A740003 for comparative purposes. For all compounds, we assessed the half-life ($t_{1/2}$) and intrinsic clearance (CLint), which predict hepatic clearance *in vivo*. The metabolic stability of compounds **5**, **9**, and A740003 is reported in Table 1. The three compounds showed distinct profiles, with A740003 being the most stable ($t_{1/2}$ = 133 min). Compound **5** had a longer half-life than compound **9**, which can be attributed to the different lipophilicities of the compounds. In fact, the cyclohexyl ring in compound **9** introduces "soft spots" that can contribute to its metabolic liability. Interestingly, both compounds **5** and **9** showed half-life values greater than 15 min, which is reported as the lower limit of predicted in vivo clearance [53]; thus, the compounds should be stable enough to be used in *in vivo* models.

2.5. Compounds 5 and 9 efficiently block the hP2X7R

Compounds **5** and **9** were tested for their inhibitory activity against hP2X7R expressed in HEK-293 cells. In this model, following stimulation with the P2X7R agonist Bz-ATP (100 μM) and measuring hP2X7R-mediated calcium influx using the fluorescent indicator FURA-2/AM [54], the IC_{50} for **5** was 370 ± 44 nM (Fig. 6A,B). The compound was administered 5 min before the stimulus with Bz-ATP and was present throughout the entire stimulation period. In the same cellular model, **5** also inhibited ethidium bromide uptake, thereby efficiently antagonizing the opening of the large, unselective macropore associated with P2X7R (Fig. 6C). With a computed IC_{50} of 47 ± 1,4 nM, **9** showed even more promising results as a hP2X7R negative allosteric modulator (Fig. 6D,E). Similarly to what was demonstrated for **5**, **9** also inhibited hP2X7R macropore formation (Fig. 6F).

2.6. 5 And 9 efficiently antagonize P2X7R activity in both human and murine cancer cells, preventing P2X7-mediated cell growth and invasiveness

To test whether compounds **5** and **9** could also act as efficient anticancer drugs, we evaluated them against various tumor cell lines using multiple *in vitro* assays commonly used to assess antitumor activity. First, we performed a Western blot analysis to detect P2X7R in murine and human cancer cell lines commonly used as preclinical cancer models. Those included B16-F10 melanoma, GL261 glioblastoma, and HCT116 colon carcinoma cells. All these cell lines expressed P2X7R (Fig. 7A) and responded to stimulation with Bz-ATP by increasing intracellular calcium (Fig. 7B-G). An effect abolished by both **5** and **9**, similarly to A740003 (Fig. 7B-G). These data confirmed not only the ability of these two drugs to antagonize the P2X7R in cancer cells but also that they are active at the mouse P2X7R, which is naturally expressed in B16-F10 and GL261 cells. The blocking ability of a compound at the mouse receptor is instrumental in the context of cancer preclinical approaches, as it enables its use in syngeneic models that are endowed with a fully functional immune system. Indeed, P2X7R plays a role in both cancer cell growth and host-mediated immune eradication or immunosuppression; therefore, it is central to test new compounds targeting it in models that account for their effects on the immune system [23,27]. Of further interest, none of the inhibitors tested, including A740003, completely abolished Ca^{2+} entry consequent to Bz-ATP stimulation in HCT116 human colon carcinoma cells, suggesting that these cells may also express the P2X1 or P2X3 receptor, at which Bz-ATP acts as an agonist too (Fig. 7F) [39]. Once it was established that **5** and **9** could both block the P2X7R in cancer cells, we performed a series of experiments to test their antitumor potential. First, we tested whether these molecules could reduce cell growth *in vitro* in a P2X7R-dependent manner. When we administered 5 μM **5, 9** or A740003 to HEK-293 cells stably expressing the hP2X7R, all molecules were able to significantly reduce cell growth after 48 h of treatment, while they showed no effect on the proliferation rates of HEK-293 cells transfected with an empty vector (mock) (Fig. 8A). We confirmed the proliferative activity conferred by hP2X7R expression [11,47] in HEK-293 cells, whose numbers were almost doubled at 48 h compared to mock controls. Data in line with those of HEK-293 hP2X7 were also obtained when testing the compounds on B16-F10 murine melanoma cells (Fig. 8B), a model widely used for *in vitro* and *in vivo* testing of the role of P2X7R in cancer growth and progression [11,14,56,57]. Since P2X7R has been implicated in the progression and poor prognosis of gliomas [55,58,59] and colon carcinoma [23], we also tested the effects of **5** and **9** in cell lines derived from these neoplasias. In the case of GL261 murine glioma (Fig. 8C) and HCT116 human colon carcinoma cells (Fig. 8D), both **5** and **9** inhibited proliferation comparably to A740003 at the same concentration after 48 h of incubation. These data also confirmed the importance of P2X7R in growth processes associated with glioma and colon carcinoma. Since P2X7R antagonism has been shown to reduce not only cancer growth and vascularization but also cell motility and *in vivo* metastatic dissemination [18,23], we tested the ability of our compounds to reduce cancer cell invasion *in vitro* (Fig. 9A-C). The experiments were performed using an assay that measures the gelatinase/collagenase activity of matrix metalloproteases released by cancer cells. These enzymes are central to the invasion and metastasis of neoplastic cells. Both **5** and **9** significantly reduced the invasive properties of all tested cell lines at 24 h of incubation (Fig. 9A-C). Notably, compound **5** showed increased gelatinolytic activity compared not only to vehicle but also to A740003 (Fig. 9A-C), which is effective in reducing cancer cell growth and dissemination, both *in vitro* and *in vivo* [18,27,60]. Similarly, compound **9** was more effective than A740003 in glioma and colon carcinoma cells (Fig. 9B,C), suggesting better antitumoral activity of both compounds compared to established P2X7R blockers. Moreover, to our knowledge, this is the first demonstration that P2X7R blockade can inhibit extracellular matrix invasion by these cancer cells using a gelatinase/collagenase assay, consistent with the receptor's reported ability to mediate the release of matrix metalloproteases [7,61,62]. Our findings also open the way to the use of **5** and **9** as potential new drugs to prevent or cure excessive wound healing, which is also known to be mediated by gelatinases and collagenases [63]. Recently, we have associated the invasive and metastatic capabilities of tumor cells with their exposure to extracellular vesicles released upon stimulation of the P2X7R (P2X7-VS) [18,23]. Furthermore, we demonstrated that inhibition of P2X7R can reverse the pro-tumorigenic effects of P2X7-VS, thereby identifying it as a novel potential therapeutic target for blocking pro-tumor extracellular vesicles [23]. For this reason, we

Table 1
Half-life and intrinsic clearance of compounds **5**, **9**, and A740003.

Compound	$t_{1/2}$ (min)	CL_{int} (μL/min/mg)
5	58	11.9
9	31	22.3
A740003	133	5.2

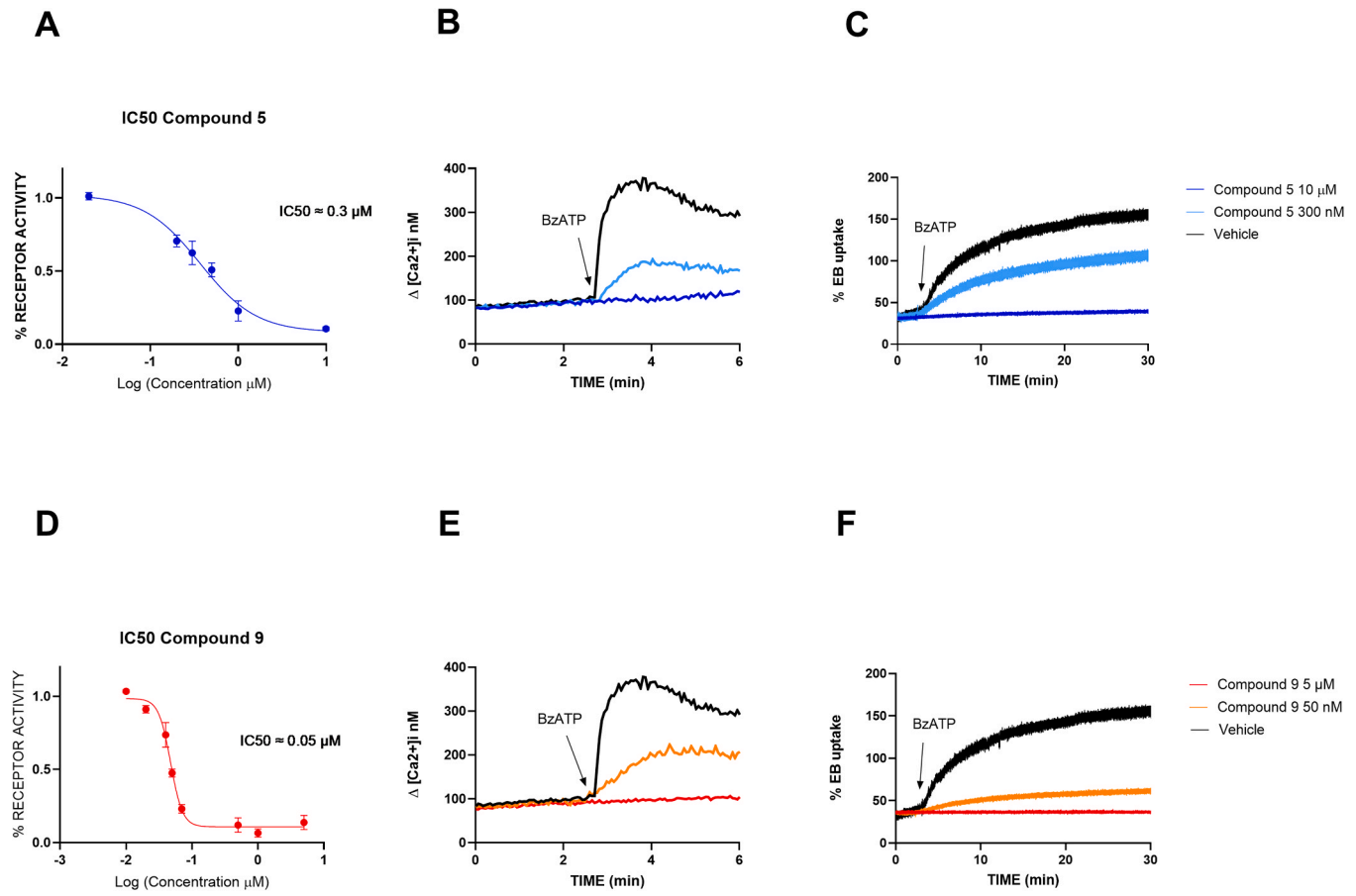

Fig. 6. Characterization of the inhibitory activity of compounds **5** and **9** at hP2X7R. (A) IC_{50} of compound **5** (n = 3); (B) Representative traces of intracellular calcium variations following the application of 100 μM Bz-ATP in the presence of vehicle (DMSO 0.0005%) or compound **5** at 10 or 0.3 μM (n = 3); (C) Ethidium bromide uptake assay, following the application of 100 μM Bz-ATP, in the presence of vehicle (DMSO 0.0005%) or compound **5** at 10 or 0.3 μM (n = 3); (D) IC_{50} of compound **9** (n = 3); (E) Representative traces of intracellular calcium variations following the application of 100 μM Bz-ATP in the presence of vehicle (DMSO 0.0005%) or compound **9** at 5 or 0.05 μM (n = 3); (F) Ethidium bromide uptake assay following the application of 100 μM Bz-ATP in the presence of vehicle (DMSO 0.0005%) or compound **9** at 5 or 0.05 μM (n = 3). Colour coding: black, vehicle; blue, **5** 10 μM, light blue, **5** 0.3 μM; red, **9** 5 μM; orange, **9** 0.05 μM.

also tested compounds **5** and **9** to evaluate their ability to inhibit the release of P2X7-VS from tumor cells. Fig. 9D shows that both compounds effectively reduced the release of P2X7-VS from B16-F10 cells to an extent comparable to that achieved with A740003. These findings are particularly interesting from a translational perspective, as although extracellular vesicles are well known to promote cancer progression and metastasis, no inhibitors targeting their release are currently available on the market [64,65]. Moreover, the ability to specifically block extracellular vesicles released within an ATP-rich microenvironment, such as the TME [66], would enable selective targeting of pro-tumorigenic vesicles without interfering with the physiological functions of other extracellular vesicle subsets.

2.7. Compounds 5 and 9 efficiently reduce melanoma growth in vivo, modifying intratumoral levels of INF-γ, TGF-β, IL1-β, and VEGF

In a final set of experiments, we tested the efficacy of **5** and **9** in reducing B16-F10 cancer cell growth *in vivo* in a primary tumor model obtained by subcutaneous injection of B16-F10 melanoma cells in C57bl/6 syngeneic mice (Fig. 10). Of interest, when administered intraperitoneally at a 2 mg/kg concentration, both drugs showed a good capacity to reduce cancer growth, comparable to that of A740003 administered at the same concentration (Fig. 10A,B). A740003 has been demonstrated to be a good antineoplastic drug in the same model [11, 27,60], and **5** seemed to reduce cancer growth more efficiently than A740003, albeit the difference was not significant (Fig. 10A). No apparent side effects were observed in mice undergoing treatment with any of the P2X7R antagonists tested. We finally measured the levels of cytokines and growth factors associated with P2X7R activity and pro-tumoral role in the literature: INF-γ, TGF-β, IL-1β, and VEGF (Fig. 10C-F). **5** And **9** significantly increased the levels of IFN-γ, which is the prototypical tumor-eradicating inflammatory cytokine in melanoma [67], suggesting that the reduced cell growth observed could, at least in part, be mediated by an increase in antitumoral immune cell activation. Of interest, **5** caused a rise in INF-γ significantly higher than A740003 (Fig. 10C). In contrast, TGF-β, a known immunosuppressive and tumor-promoting growth factor [68], was significantly reduced by all administered compounds (Fig. 10D). Interestingly, also in this case, **5** proved more effective in reducing TGFβ than A740003, and even **9** (Fig. 10D). All tested drugs substantially reduced IL-1β in a comparable manner (Fig. 10E). These data were not surprising, given the central role of P2X7R in the maturation and secretion of this cytokine [21]. Finally, in the case of VEGF, which is a growth factor promoting neo-vascularization, while both **5** and **9** reduced the levels as compared to placebo, **5** was less efficient of both **9** and A740003 in decreasing the concentration of the growth factor (Fig. 10F), thus suggesting that this compound could be less efficient in preventing new vessels formation in the tumor bed. Taken together, these data suggest that both **5** and **9** are promising candidates as antitumor drugs, with **5** potentially more effective at reducing the metastatic potential of cancer cells, increasing immune cell infiltration, and eradicating tumors, while reducing immunosuppression in the TME. In contrast, the second could prove

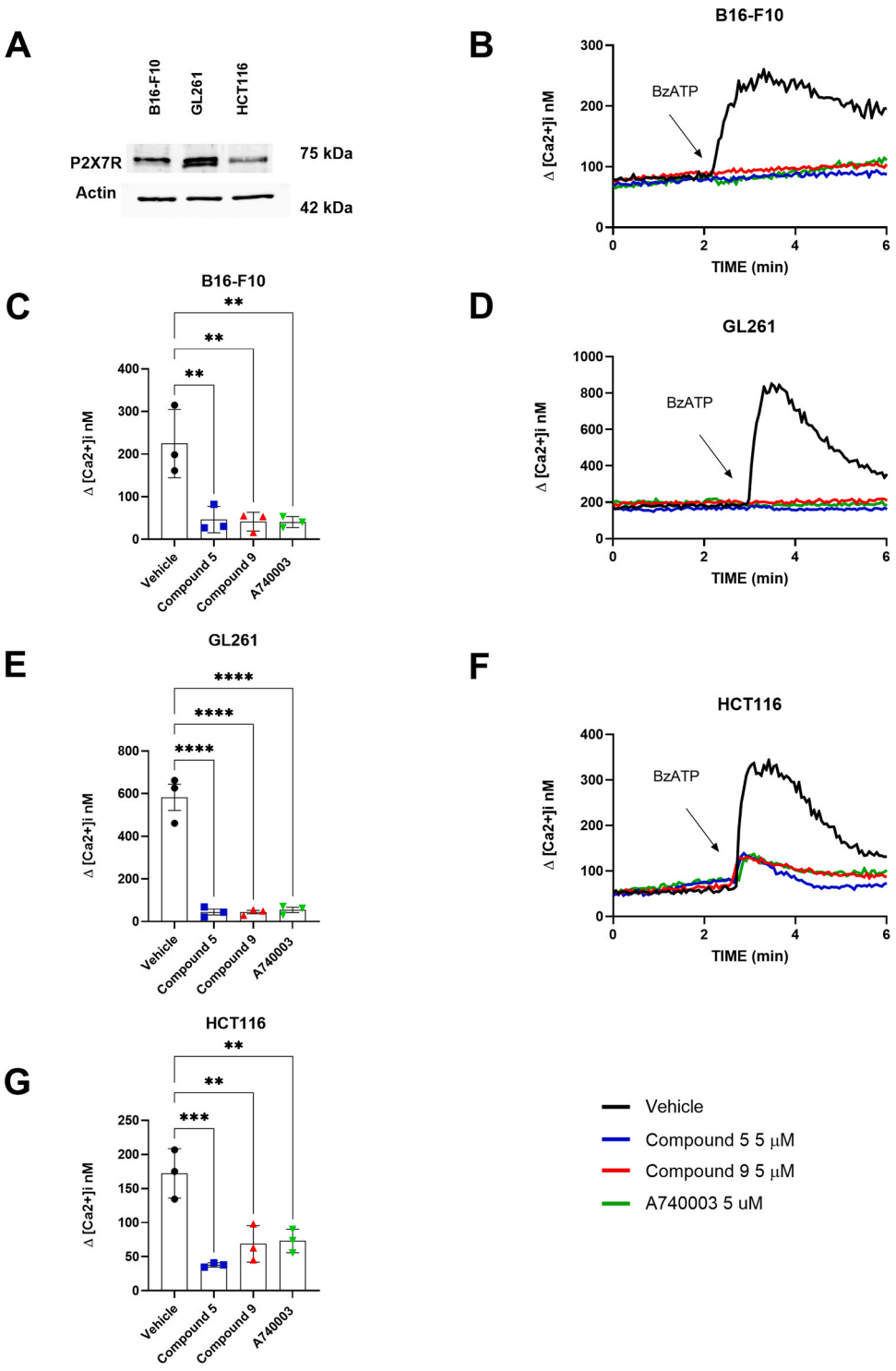

Fig. 7. Compounds **5** and **9** reduce P2X7R activity on different tumoral cell lines. (A) Immunoblot, showing the expression of P2X7R in B16-F10 (murine melanoma), GL261 (murine glioblastoma) and HCT116 (human colon carcinoma) cells. (B, D, F) Representative traces of intracellular calcium variations following stimulation with 100 μM BZ-ATP. (C, E, G) Variation of intracellular calcium concentrations ($[Ca^{2+}]_i$) following P2X7R stimulation. All cells were preincubated with the different compounds at 5 μM or with vehicle (DMSO 0.0005%). (B, C) murine melanoma B16-F10 cells, (D, E) murine glioblastoma GL261 cells (F, G) human colon carcinoma cells HCT116. Colour coding: black vehicle; blue compound **5**, red compound **9**; green A740003.

more efficacious in preventing tumor neovascularization.

3. Conclusion

Compounds **5** and **9** emerge as potent, selective P2X7R antagonists with strong anticancer properties. Both agents show high receptor affinity, effectively block P2X7R-dependent signalling, and are metabolically stable. In cancer cells, they reduce proliferation, invasiveness, and P2X7R-mediated extracellular vesicle release. *In vivo*, both compounds significantly inhibit melanoma growth and favourably modulate the tumour microenvironment by increasing antitumoral IFN-γ and reducing protumorigenic TGF-β, IL-1β, and VEGF. Together, these

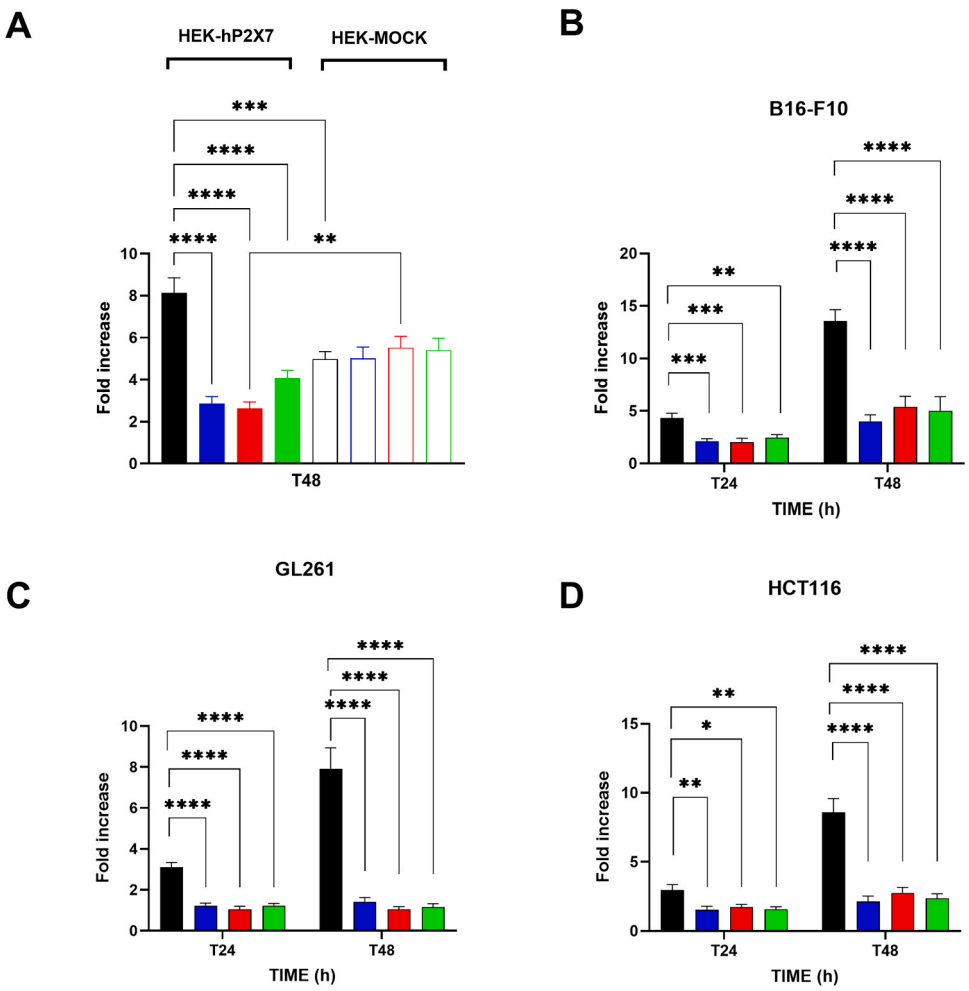

Fig. 8. Compounds **5** and **9** reduce cell growth in hP2X7-HEK293 and tumor cell lines. (A) HEK-293 hP2X7 and HEK-293 transfected with an empty vector (mock) cells were treated with compound **5**, compound **9** or A740003 (all at a 5 μM concentration) and counted at time 0, 24 and 48 h. Data are presented as cell numbers fold increase on time 0 (N = 3). (B-D) B16-F10, GL261, and HCT116 cells (respectively murine melanoma, murine glioblastoma and human colon carcinoma cells) were treated with compound **5**, compound **9** or A740003 (all at a 5 μM concentration) and counted at time 0, 24 and 48 h of incubation. Data are shown as the mean ± SD, * $p < 0.05$, ** $p < 0.01$, *** $p < 0.001$, ****$p < 0.0001$.

results identify compounds **5** and **9** as promising lead molecules for developing P2X7R-targeted anticancer therapies.

4. Experimental

4.1. Chemistry

All reagents, solvents or silica were purchased from Merck (Milan, Italy), Organics BV (Fisher Scientific GmbH, Geel, Belgium), Carlo Erba (Cornaredo, Italy), and used, unless otherwise stated, without further purification. Thin-layer chromatography (TLC) was carried out on pre-coated TLC plates with silica gel 60 F254 (Merk Life Science S.r.l., Milan, Italy). Column chromatography was performed with Merck silica gel 60 Å (40–63 μm) as the stationary phase.

Melting points were determined with a Büchi apparatus and are uncorrected. ^{1}H NMR spectra were recorded on a Bruker Ascend 500 MHz spectrometer (Bruker Italia S.r.l., Milan, Italy). All chemical shift values are reported in ppm (δ), and coupling constant values are reported in Hz (*J*). Mass spectra were recorded on an HPLC Alliance 2695 (Waters, Milford, MA, USA). Elemental analyses were determined on a Fisons Instruments Model EA 1108 CHNS-O model analyzer. Purity of the compounds is > 98%.

1-(2,3-Dichlorophenyl)-1*H*-1,2,4-triazole (**2**): A mixture of **1** (5.6 mmol, 1000 mg) and formamide used as solvent (54 mL) was heated in a sealed steel vial up to 150 °C for 16 h. Subsequently, the reaction mixture was partitioned between H_2O and EtOAc/EtOAc and the organic layer was washed with brine and a saturated NaCl solution. The organic phase was dehydrated over Na_2SO_4, then filtered and evaporated; the residue obtained was purified by flash column chromatography eluting with n-Hex-EtOAc (98:2–80:20) to obtain compound **2** (4.45 mmol, 944 mg; yield 79%). ^{1}H-NMR ($CDCl_3$) δ: 7.59 (t, J = 7.12 Hz, 1H, Ph) 7.65 (d, J = 7.15 Hz, 1H, Ph), 7.88 (d, J = 7.10 Hz 1H, Ph), 8.30 (s, 1H, CH). ESI-MS positive ion mode m/z: $[M+H]^+$: 214.0. Elemental analysis calcd for $C_8H_5Cl_2N_3$: C, 45.10; H, 2.36; N, 19.73. Found: C, 45.15; H, 2.40; N, 19.70.

5-Bromo-1-(2,3-dichlorophenyl)-1*H*-1,2,4-triazole (**3**): To a solution of **2** (3.3 mmol, 700 mg) in CCl_4 (15 mL), NBS (9.9 mmol, 1761 mg) and benzoyl peroxide (BPO) (0.165 mmol, 40 mg) were added and reacted at 80 °C for 24 h. Then, the volatile compounds were evaporated, and the residue was purified by flash column chromatography eluting with c-Hex-EtOAc (98:2–94:6) to obtain **3** (1.98 mmol, 578 mg; 60% yield) as a white powder. ^{1}H-NMR ($CDCl_3$) δ: 7.38 (m, 2H, H-Ph), 7.72 (m, 1H, H-Ph), 8.10 (s, 1H, CH). ESI-MS positive ion mode m/z: $[M+H]^+$: 293.7. Elemental analysis Calcd for $C_8H_4BrCl_2N_3$: C, 32.77; H, 1.37; N, 14.35. Found: C, 32.80; H, 1.39; N, 14.30.

1-(2,3-Dichlorophenyl)-*N*-(2,2-diphenylethyl)-1*H*-1,2,4-triazole-5-amine (**4**): Intermediate **3** (0.34 mmol, 100 mg) and 2,2-diphenylethylamine (1.71 mmol, 338 mg) were placed in a Parr bomb and

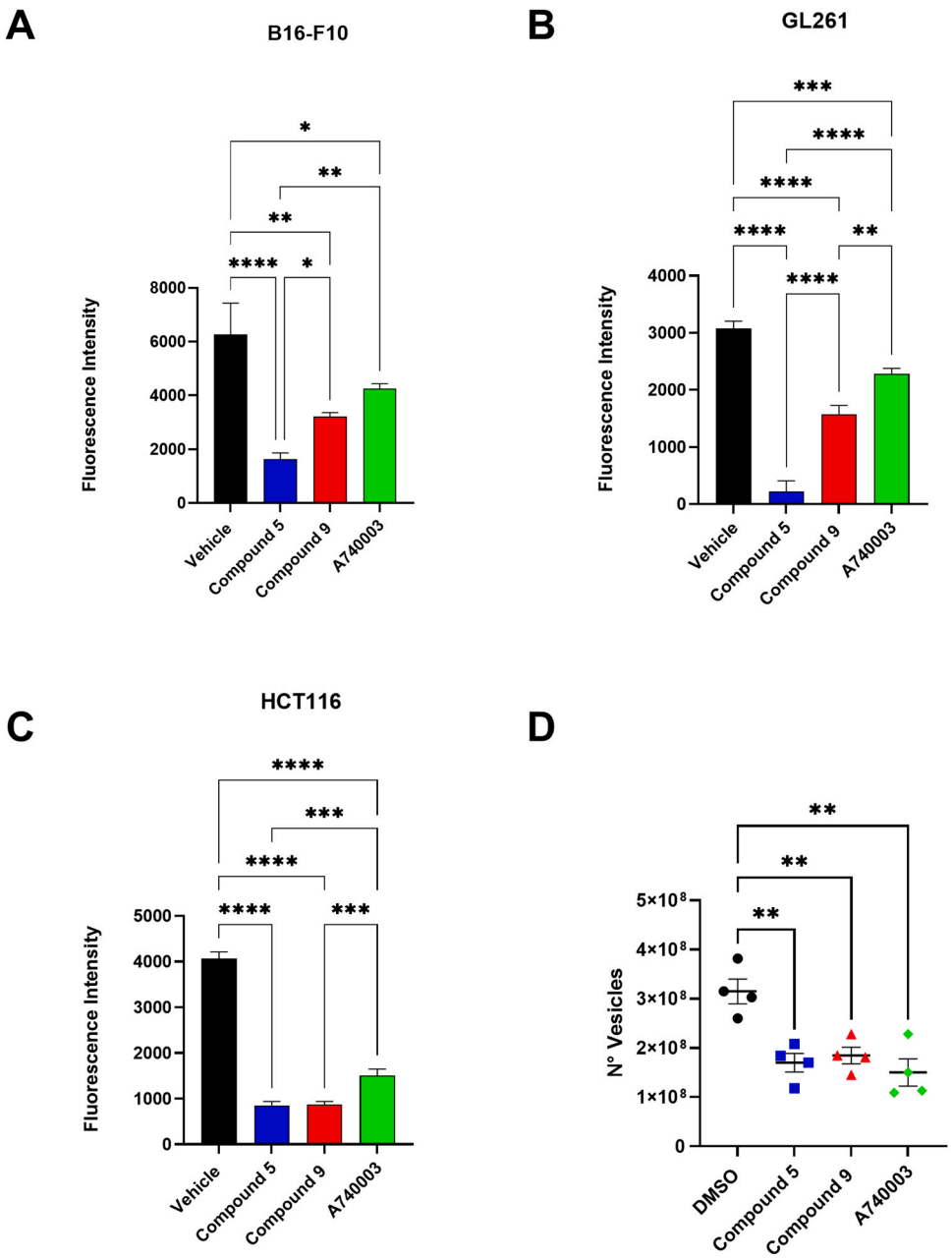

Fig. 9. Compounds **5** and **9** reduce the invasiveness of melanoma, glioblastoma, and colon cancer cells. (A) DQ-gelatin assay performed on murine melanoma cell line (B16-F10), treated with compound **5**, compound **9**, the commercial P2X7R antagonist A740003 (all at a 5 μM concentration) or vehicle (DMSO 0.0005%) for 48 h; (B) DQ-gelatin assay performed on murine glioblastoma cell line (GL261), treated with compound **5**, compound **9**, A740003 (all at a 5 μM concentration) or vehicle for 48 h. (C) DQ-gelatin assay performed on human colon cancer cell line (HCT116), treated with compound **5**, compound **9**, A740003 (all at a 5 μM concentration) or vehicle for 48 h. (D) Vesicles were collected following a 15-minute stimulation of B16-F10 cells with 100 μM Bz-ATP, in the presence of compounds **5**, **9**, A740003 (all at a 5 μM concentration), or vehicle (DMSO 0.0005%). Color coding: black, vehicle, blue compound **5**; red compound **9**, green A740003. Data are shown as the mean ± SD. * $p < 0.05$, ** $p < 0.01$, *** $p < 0.001$. **** $p < 0.0001$.

reacted by melting at 140 °C for 12 h. The residue, transferred to a round-bottom flask, was purified by flash column chromatography, eluting with n-Hex-EtOAc (95:5–80:20). Derivative 4 (0.01 mmol, 5 mg; 4% yield) was obtained after crystallization from isopropanol. M.p.: 116–118 °C. ^{1}H-NMR ($CDCl_3$) δ: 4.21 (brs, 2H, CH_2), 4.38 (m, 1H, CH), 7.09 (d, J = 7.15 Hz, 1H, H-Ph), 7.26 (m, 11H, H-Ph), 7.65 (d, J = 7.10 Hz, 1H, H-Ph), 7.73 (s, 1H, H-Triazole). ESI-MS positive ion mode m/z: $[M+H]^+$: 408.9, $[M+Na]^+$: 430.8. Elemental analysis Calcd for $C_{22}H_{18}Cl_2N_4$: C, 64.56; H, 4.43; N, 13.69. Found: C, 64.60; H, 4.42; N, 13.60.

1-(2,3-Dichlorophenyl)-*N*-(benzyl)-1*H*-1,2,4-triazole-5-amine (5): Intermediate **3** (0.34 mmol, 100 mg) and benzylamine (0.85 mmol, 92 μL) were placed in a Parr bomb and reacted by melting at 140 °C for 12 h. The residue, transferred in a round-bottom flask, was purified by flash column chromatography eluting with n-Hex-EtOAc (95:5–80:20). **5** (0.07 mmol, 22 mg; 20% yield) was obtained after crystallization using isopropanol. M.p.: 113–114 °C. ^{1}H-NMR ($CDCl_3$) δ: 4.26 (brs, 2H, CH_2), 4.65 (m, 1H, CH), 7.31 (m, 1H, H-Ph), 7.36 (m, 6H, H-Ph), 7.61 (d, J = 7.10 Hz, 1H, H-Ph), 7.63 (d, J = 7.10 Hz, 1H, H-Ph), 7.73 (s, 1H, H-Triazole). ESI-MS positive ion mode m/z: $[M+H]^+$: 320.1, $[M+Na]^+$: 342.2. Elemental analysis Calcd for $C_{15}H_{12}Cl_2N_4$: C, 56.43; H, 3.79; N, 17.55. Found: C, 56.49; H, 3.80; N, 17.45.

2-Chloro-3-methoxybenzoic acid (7): An aqueous solution of 2-chloro-3-methoxybenzaldehyde (**6**, 0.59 mmol, 100 mg in 5 mL H_2O),

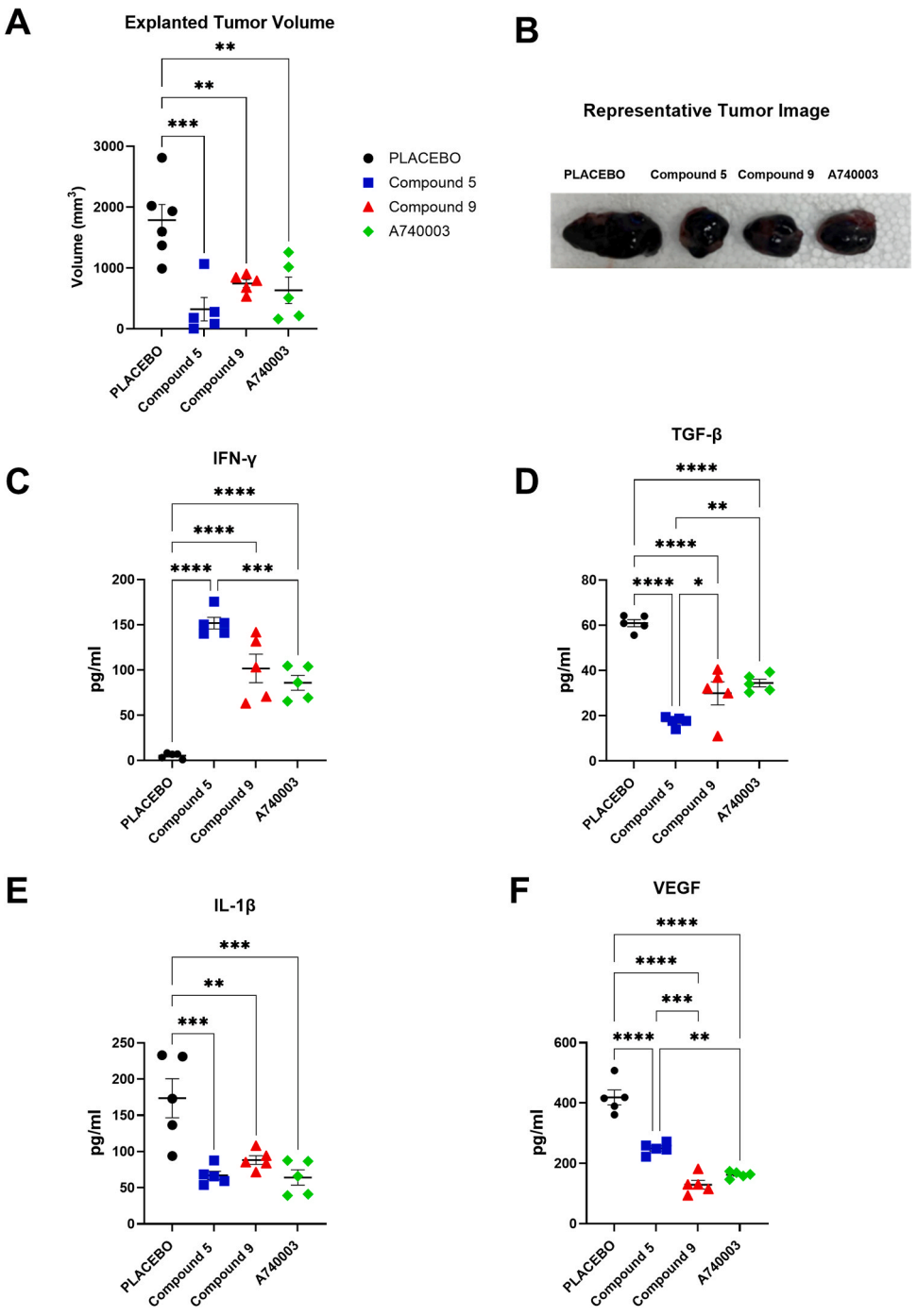

Fig. 10. Intratumoral administration of compounds **5** and **9** effectively reduces B16-F10 growth in C57bl/6, affecting cytokine and growth factor levels. Female C57bl/6 mice were subcutaneously inoculated into the fat of the inferior limb with 2,5 x 10^5 B16-F10 cells. **5**, **9**, and A740003 (each 2 mg/kg) were administered via intraperitoneal injection to mice at post-inoculum days 5, 8, 11. (A) *Ex vivo* tumor volume. (B) Representative picture of tumors from treated mice at post-inoculum day 14. (C-F) Levels of intra-tumoral cytokines and growth factors. IFN-γ (C), TGF-β (D), IL-1β (E) and VEGF (F) were evaluated in tumor-derived samples (n = 5 per group). Data are shown as the mean ± SEM. * $p < 0.05$, ** $p < 0.01$, *** $p < 0.001$. **** $p < 0.0001$.

$NaHCO_3$ (1.48 mmol, 124 mg) and $KMnO_4$ (1.77 mmol, 280 mg) was heated to 90 °C and stirred for 5 h. The mixture was then cooled to r.t., acidified to pH 4, and subsequently extracted with dichloromethane (DCM) (3 x 50 mL). The organic phases were collected, dehydrated by Na_2SO_4 then filtered and evaporated to obtain **7** (0.48 mmol, 90 mg, yield 81%) as a white powder. ^{1}H-NMR ($CDCl_3$) δ: 3.88 (s, 3H, CH_3), 7.27 (m, 2H, H-Ph), 7.38 (m, 1H, H-Ph), 13.37 (brs, 1H, OH). ESI-MS negative ion mode m/z: $[M-H]^-$: 185.1. Elemental analysis Calcd for $C_8H_7ClO_3$: C, 51.48; H, 3.78. Found: C, 51.50; H, 3.75.

2-Chloro-*N*-(2,2-diphenylethyl)-3-methoxybenzamide (8): **7** (0.53 mmol, 100 mg) was dissolved in anhydrous DMF (5 mL) and reacted with EDC (0.80 mmol, 153 mg), HOBt (0.80 mmol, 108 mg), and DIPEA (1.60 mmol, 278 μL) for 1 h at r.t. Then, 2,2-diphenylethylamine (0.53 mmol, 104 mg) was added and allowed to react at r.t. for 12 h. Volatiles were evaporated to dryness, and the residue was purified by flash column chromatography eluting with n-Hex-EtOAc (90:10–70:30) to afford the final **8** (0.10 mmol, 36 mg; 20% yield). M.p.: 121–124 °C. ^{1}H-NMR ($CDCl_3$) δ: 4.15 (m, 2H, CH_2), 4.37 (m, 1H, CH), 6.05 (brs, 1H, NH), 6.97 (d, $J = 7.20$ Hz, 1H, H-Ph), 7.10 (d, $J = 7.15$ Hz, 1H, H-Ph), 7.30 (m, 11H, H-Ph). ESI-MS positive ion mode m/z:

$[M+H]^+$: 366.3, $[M+Na]^+$: 388.2. Elemental analysis Calcd for $C_{22}H_{20}ClNO_2$: C, 72.20; H, 5.51; N, 3.83. Found: C, 72.25; H, 5.57; N, 3.80.

2-Chloro-*N*-(2-cyclohexyl-2-phenylethyl)-3-methoxybenzamide (9): **7** (0.53 mmol, 100 mg) was dissolved in anhydrous DMF (5 mL) and reacted with EDC (0.80 mmol, 153 mg), HOBt (0.80 mmol, 108 mg), and DIPEA (1.60 mmol, 278 μL) for 1 h at r.t. After this time, **12** (0.53 mmol, 107 mg) was added and allowed to react at r.t. for 12 h. Volatiles were evaporated to dryness, and the residue was purified by flash column chromatography eluting with n-Hex-EtOAc (90:10–70:30) to afford the final compound **9** (0.14 mmol, 52 mg; 26% yield). M.p.: 120–123 °C. ^{1}H-NMR ($CDCl_3$) δ: 0.88 (m, 1H, CH), 1.14 (m, 4H, 2 x CH_2), 1.27 (m, 1H, CH), 1.57 (m, 1H, CH), 1.61 (m, 2 H, CH_2), 1.78 (m, 1H, CH), 2.02 (m, 1H, CH); 2.60 (m, 1H, CH), 3.48 (m, 1H, CH_2), 3.85 (s, 3H, CH_3), 4.49 (m, 1H, CH), 5.77 (brs, 1H, NH), 6.93 (d, 1H, H-Ph), 7.02 (d, J = 7.15 Hz, 1H, H-Ph), 7.19 (m, 6H, H-Ph). ESI-MS positive ion mode m/z: $[M+H]^+$: 371.9, $[M+Na]^+$: 393.9. Elemental analysis Calcd for $C_{22}H_{26}ClNO_2$: C, 71.03; H, 7.04; N, 3.77. Found: C, 71.17; H, 7.09; N, 3.71.

***N*-((2-(azetidin-1-yl)pyridin-3-yl)methyl)-2-chloro-3-methoxybenzamide (10)**: **7** (0.32 mmol, 60 mg) was dissolved in anhydrous DMF (5 mL) and reacted with EDC (0.48 mmol, 92 mg), HOBt (0.48 mmol, 65 mg), and DIPEA (0.96 mmol, 167 μL) for 1 h at r.t. The 2-chloro-3-methoxybenzamine (0.32 mmol, 52 mg) was then added and allowed to react at r.t. for 12 h. Volatiles were removed under vacuum, and the residue was purified by flash column chromatography eluting with n-Hex-EtOAc (30:70–70:30); further purification was performed by preparative TLC eluted with n-Hex-EtOAc (60:40). Compound **10** (0.039 mmol, 13 mg; 12% yield) was obtained as a white solid. M.p.: 124–126 °C.^{1}H-NMR ($CDCl_3$) δ: 2.36 (m, 2H, CH_2), 3.90 (s, 3H, CH_3), 4.21 (m, 4H, 2 x CH_2), 4.58 (d, J = 15.1 Hz, 2H, CH_2), 6.50 (brs, 1H, NH) 6.70 (t, J = 15.1 Hz, 1H, H-Ph), 7.08 (d, J = 15.1 Hz,1H, H-Ph), 7.25 (d, J = 15.1 Hz, 1H, H-Ph), 7.31 (m, 1H, H-Ph), 7.52 (d, J = 15.1 Hz,1H, H-Ph), 8.13 (d, J = 15.1 Hz, 1H, H-Ph). ESI-MS positive ion mode m/z: $[M+H]^+$: 332.1, $[M+Na]^+$: 354.0. Elemental analysis Calcd for $C_{15}H_{16}ClN_3O_2$: C, 56.67; H, 5.07; N, 13.23. Found: C, 56.70; H, 5.09; N, 13.20.

2-Cyclohexyl-2-phenylethan-1-amine (12): To a solution of 2-cyclohexyl-2-phenylacetonitrile (**11**, 2.2 g, 11 mmol) in EtOH (50 mL) were added 4 mL of concentrated HCl and 200 mg of 10% Pd/C. The mixture was placed in a H_2 atmosphere (60 psi) for 12 h. After filtering off the catalyst, the volatiles were evaporated, and the residue was purified on a flash column chromatography by eluting with $CHCl_3$-MeOH (97:3) to obtain **12** (1.83 g 9 mmol) as a white solid in 82% yield. ^{1}H-NMR (DMSO) δ: 0.89 (m, 2H, CH_2), 1.02 (m, 2H, CH_2), 1.08 (m, 2H, CH_2), 1.11 (m, 2H, CH_2), 1.18 (m, 2H, CH_2), 1.35 (m, 1H, CH), 1.79 (m, 2H, CH_2N), 3.13 (m, 1H, CHPh), 7.28 (m, 2H, H-Ph), 7.29 (m, 1H, H-Ph), 7.31 (m, 2H, H-Ph), 7.35 (brs, 2H, NH_2). ESI-MS positive ion mode m/z: $[M+H]^+$: 204.3. Elemental analysis Calcd for $C_{14}H_{21}N$: C, 82.72; H, 10.41; N, 6.87. Found: C, 82.81; H, 10.49; N, 6.79.

2-(Azetidin-1-yl)nicotinonitrile (14): To a solution of 2-fluoronicotinonitrile (**13**, 13.10 mmol, 1.6 g) in THF (15 mL), Et_3N (65.5 mmol, 9 mL) and azetidine hydrochloride (59.81 mmol, 1130 mg) were added at 0 °C, then slowly warmed to r.t. and allowed to react for 16 h. The volatiles were removed under vacuum, H_2O was added to the residue and the mixture was extracted with DCM (3 x 50 mL). The organic phases were collected, dried over anhydrous Na2SO4, filtered, and evaporated. The residue was purified by crystallization using EtOAc/c-Hex to give **14** (12.6 mmol, 2.024 mg; 96% yield). ^{1}H-NMR ($CDCl_3$) δ: 2.43 (m, 2H, CH_2), 4.37 (t, J = 7.15 Hz, 4H, CH_2-N x 2), 6.59 (m, 1H, H-Ph), 7.65 (m, 1H, H-Ph), 8.28 (m, 1H, H-Ph). ESI-MS positive ion mode m/z: $[M+H]^+$: 160.2. Elemental analysis Calcd for $C_9H_9N_3$: C, 67.92; H, 5.70; N, 26.38. Found: C, 67.99; H, 5.72; N, 26.35.

(2-(Azetidin-1-yl)pyridin-3-yl)methanamine (15): Compound **14** (200 mg; 1.25 mmol) was dissolved in 7 N methanolic ammonia (5 mL), freshly prepared Ni/Raney was added as a catalyst, and the mixture was placed under H_2 atmosphere (60 psi) at 50 °C for 6 h. After filtration through celite the residue was purified by flash column chromatography, eluting with DCM-NH_3/MeOH 7 N sol. (98:2–90:10) to afford **15** (1.08 mmol, 176 mg; 87% yield) as a light-yellow solid. ^{1}H-NMR ($CDCl_3$) δ: 2.36 (m, 2H, CH_2), 3.76 (s, 2H, CH_2-NH_2), 4.15 (t, J = 7.10 Hz, 4H, CH_2N x 2), 6.70 (m, 1H, H-Ph), 7.44 (m, 1H, H-Ph), 8.13 (m, 1H, H-Ph). ESI-MS positive ion mode m/z: $[M+H]^+$: 164.2. Elemental analysis Calcd for $C_9H_{13}N_3$: C, 66.26; H, 8.02; N, 25.72. Found: C, 66.30; H, 8.05; N, 25.70.

4.2. Molecular Modeling

Homology modeling and docking studies were performed within MOE (Molecular Operating Environment) software suite interface [50]. The recently reported electron cryomicroscopy (cryo-EM) structure of the hP2X7R in complex with the allosteric inhibitor UB-ALT-P30 (PDB code: 9E3O [49]) was retrieved from the Protein Data Bank and checked within MOE. For the homology modeling experiment, the experimental 3D structures of the rat P2X7R obtained by cryo-EM in complex with its allosteric inhibitor A-839977 (PDB code: 8TR7 [51]) were retrieved from the Protein Data Bank (http://www.rcsb.org). Homology Modeling protocols available in MOE were used to develop a 3D model of hP2X7R based on the 8TR7 structure as a template. The obtained structures were then used as targets for docking studies of the compounds developed in this study. MOE docking and scoring tools, as well as energy minimization tools, were employed. The top-scoring conformations for each compound were selected for final energy minimization, visualization, and analysis.

4.3. Biological assays

4.3.1. Cell cultures

HEK-293 cells stably transfected with the recombinant human P2X7R or the empty vector (mock) were previously available at Adinolfi's laboratory [11,47] and were cultured in DMEM-F12 medium. B16-F10 murine melanoma (ATCC CRL-6475), GL261 murine glioblastoma (Cytion GmbH, Heidelberg, Germany), and HCT116 human colon carcinoma (EP-CL-0096, CliniScience, Amsterdam, Netherlands) cell lines were cultured in RPMI-1640, DMEM-F12, and McCoy's media, respectively. All media were purchased from Euroclone and supplemented with 10% fetal bovine serum, 100 U/mL penicillin, and 100 mg/mL streptomycin (Euroclone, Milan, Italy). The cells were periodically tested for contamination using the Mycoplasma detection kit from Applied Biological Materials (Richmond, Canada).

4.3.2. Binding assay at hP2X7

HEK-293 hP2X7R cell membranes for binding assays were prepared by mechanically detaching the cells from the petri dish and suspending them in a cold hypotonic buffer (5 mM Tris/HCl, 2 mM EDTA, pH 7.4). The cell suspension was homogenized (Ultra-Turrax, 2 × 15 s at maximum speed) and the homogenate centrifuged for 10 min (4 °C) at 1000 g. The supernatant was subsequently centrifuged for 30 min (4 °C) at 100,000 g, and the pellet containing the membrane proteins was resuspended in 50 mM Tris/HCl, pH 7.4. The amount of protein in the suspension was determined by the Bradford method using the BCA Protein Assay Kit (Pierce). The samples were then frozen in liquid nitrogen and stored at −80 °C.

Dissociation constants (K_D-value) of [^{3}H]-JNJ-64413739 (RC Tritec AG, Teufen, Swiss) were measured in saturation binding experiments.

The increasing concentrations of the radioligand (from 0.25 to 60 nM) were incubated in a total volume of 250 μL containing 25 μg of membrane proteins in the specific buffer. The non-specific binding was determined in the presence of JNJ-47965567 100 μM (Cat. N. 5299, Tocris). The samples were incubated for 3 h at room temperature, filtered into a 96-well filter plate (UniFilter GF/C, Perkin-Elmer) using the FilterMate Cell Harvester (Perkin-Elmer), and washed 3 times with

cold distilled water. After drying the filter plate at 40 °C for 30′, 20 μL of scintillating liquid (Microscint-20, Perkin-Elmer) was added to each well, and then the radioactivity was quantified with the MicroBeta^2 Scintillation Counter (Perkin-Elmer). All binding data were fit to nonlinear regression curves using GraphPad Prism 8 (GraphPad Software, San Diego, CA, USA).

Following the saturation assay, a set of competition-binding assays was performed to determine Ki values for the synthesized compounds. The understudy compounds were incubated at varying concentrations with 1 nM [^{3}H]-JNJ-64413739 and 25 μg of membrane proteins, in a final volume of 200 μL. Non-specific binding was assessed in the presence of 100 μM JNJ-47965567. As in saturation experiments, the samples were incubated for 3 h, filtered and washed. The dried plate was supplemented with 20 μL of scintillation fluid (Microscint-20), and the radioactivity was quantified with the MicroBeta^2 Scintillation Counter. The K_i values of the compounds under investigation were determined by fitting nonlinear regression curves using GraphPad Prism 8 [69].

4.3.3. *In vitro metabolic stability assay*

Metabolic stability in mouse liver microsomes was assessed as previously reported [70] by incubating in 100 mM potassium phosphate buffer (pH 7.4) and at 37 °C mouse liver microsomes (1.0 mg/mL microsomal protein, Tebu-Bio, Milan, Italy), test compounds (10 μM) and the NADPH regenerating system (50 mM glucose-6-phosphate, 10 unit/mL glucose-6-phosphate dehydrogenase, 10 mM NADP, final glucose-6-phosphate dehydrogenase concentration of 1 U/mL) (Tebu--Bio, Milan, Italy). Samples were removed at specific time points (0, 5, 15, 30, 60, and 120 min) and quenched with an equal volume of cold acetonitrile containing the internal standard. Test compounds incubated with microsomes without the NADPH regenerating system were included. Quenched samples were centrifuged at 5000 x g for 15 min. The supernatants (20 μL) were analyzed by HPLC with an Agilent 1260 Infinity Binary LC System equipped with a diode array detector (chromatographic data were analyzed with the Open Lab software) and a Phenomenex Synergi Fusion-RP column (100 mm x 3 mm, 4 μm particle size). The samples were separated by gradient elution (phase A water, phase B ACN; gradient from 10% to 100% B in 10 min) at 0.7 mL/min. Quantification of concentrations was done by measuring the area under the peak.

In vitro half-life ($t_{1/2}$) was calculated with the expression $t_{1/2}$= 0.693/b, where b is the slope found in the linear fit of the natural logarithm of the fraction remaining of the parent compound versus the incubation time. The intrinsic clearance (CL_{int}) was then calculated following the equation:

$$CL_{int} = \frac{0.693}{\text{in vitro } t_{1/2}} \times \frac{1}{\text{mg/mL microsomal protein}}$$

4.3.4. *$[Ca^{2+}]_i$ measurements*

Intracellular calcium concentration variations were measured with the fluorescent indicator FURA-2/AM (Invitrogen-Thermo Fisher Scientific) with a Cary Eclipse spectrophotometer (Agilent Technologies, Milan, Italy) as previously described [54]. Briefly, 2 × 10^6 cells were loaded with 2 μM FURA-2/AM for 20 min in the following solution: 125 mM NaCl, 5 mM KCl, 1 mM $MgSO_4$, 1 mM NaH_2PO_4, 20 mM Hepes, 5,5 mM glucose, 5 mM $NaHCO_3$, 1 mM $CaCl_2$, 250 μM sulfinpyrazone, pH 7.4. Cells were then washed and resuspended in the same solution containing the required compounds at different concentrations. Following a 10-minute pre-incubation, cells were loaded into a quartz cuvette, and fluorescence emission was recorded at 505 nm with excitation wavelengths of 340 nm and 380 nm. After a 2-minute lag to stabilize basal calcium measurements, cells were stimulated with 100 μM BZ-ATP.

4.3.5. *Ethidium bromide uptake*

Ethidium bromide uptake was monitored using a fluorescence spectrophotometer equipped with a thermostatic control system and magnetic stirring (Cary Eclipse) as previously described [71]. Briefly, 1x10^6 cells were suspended in the following solution: 300 mM sucrose, 1 mM K_2HPO_4, 1 mM $MgSO_4$, 5.5 mM D-glucose, 20 mM HEPES, 1 mM calcium, 20 μM ethidium bromide, pH 7.4 at 37°C. Cells were stimulated with 100 μM Bz-ATP in the presence or absence of P2X7R antagonists. Fluorescence emission was measured at 360 nm excitation and 580 nm emission.

4.3.6. *Immunoblot*

Cell membrane extracts were prepared as described in 4.3.2. Whole-cell lysates were obtained by resuspending the cells in RIPA Buffer (R0278, Nalgene) supplemented with HaltTM Protease and Phosphatase inhibitor cocktail, EDTA-free (Thermo Fisher). The lysates were loaded in a 10% ProteinEle Precast Tris-Glycine Gel (Transgen). Proteins were transferred on nitrocellulose membranes (Amersham Protran, GE Healthcare, United States); which were then incubated overnight at 4°C with the following primary antibodies: anti-P2X7 antibody (P8232, Sigma-Aldrich, 1:200), anti-actin antibody (A5060, Sigma-Aldrich,1:1000) and anti-PMCA4 (P1494, Sigma-Aldrich,1:1000). As secondary antibodies HRP-conjugated goat anti-rabbit (Novex, Life-technologies, A16096) or goat anti-mouse (Thermofisher, 626520), were applied at a 1:2000 dilution. Protein bands were visualised by ECL HRP Chemiluminescent Substrate WESTAR NOVA 2.0 (Cyanagen Srl, Bologna, Italy) with a Chemidoc GO IMAGING SYSTEM (BIO-RAD).

4.3.7. *Proliferation assay*

2.5 x 10^4 cells per cell type were seeded in six-well plates in their respective media (see *4.2.1*). After incubation at 37 °C for 24 h, **5**, **9**, A740003 (all at a 5 μM concentration), or vehicle DMSO were administered, and five images for each well were acquired with a DM IL Led Leica Microsystems (GmbH) microscope. Cell numbers were assessed at 0, 24, and 48 h.

4.3.8. *DQ-gelatin invasiveness assay*

15 x 10^3 cells were plated in 96-well plates, plus DQ-gelatin 1 mg/mL mixed with reaction buffer 1x (0.5 M tris-HCl, 1.5 M NaCl, 50 Nm $CaCl_2$, 2 mM sodium azide, pH 7.6). Cells were resuspended in the reaction buffer and added to the wells with either vehicle or 5 μM of the treatment. Fluorescence was assessed after 24 h, with the Wallac 1420 Multilabel Counter Viktor X3 (PerkinElmer, Finland).

4.3.9. *Extracellular vesicles quantification*

B16 cells were seeded in T25 flasks, and when they reached confluence, the medium was removed, and the cells were washed with PBS. Then they were pre-incubated with 3 mL of the solution described in 4.3.4 containing the appropriate P2X7R antagonist at 5 μM or control (PBS), and after 5 min, cells were treated with 100 μM BzATP for 15 min at 37°C with 5% CO_2. The supernatant was depleted of cells and debris by centrifugation at 2000 x g for 10 min at 4°C. Particles present in the supernatant were quantified using Videodrop Technology (Myriade).

4.3.10. *In vivo experiments*

Animal experiments were performed according to previously described protocols for administering a P2X7 antagonist in oncological models [72]. Briefly, 2.5 x 10^5 B16 melanoma cells were subcutaneously inoculated into the flank of 6-week-old female C57bl/6 mice. Mice were randomized into 4 groups of 5–6 animals each, and the operator was blinded to the allocation. They were treated every 72 h with an intraperitoneal injection of placebo (PBS + 0.0005% DMSO), **5** (2 mg/Kg), **9** (2 mg/Kg), or A740003 (2 mg/Kg). Animals were sacrificed at day 14th from the inoculum, and tumor size was assessed *ex vivo* with a calliper. Volume was calculated according to the following equation: volume = π/6 x [w1 x (w2)^2], w1 = major diameter and w2 minor diameter. All animal procedures were approved by the Organism for Animal Wellbeing (OPBA) of the University of Ferrara and the Italian Ministry of

Health, in compliance with EU Directive 2010/63/EU and Italian D. Lgs. 26/2014 and were under generally accepted guidelines for the welfare and use of animals in cancer research [73].

4.3.11. Intra-tumoral cytokines and growth factors evaluation

Tumor masses were homogenized in a lysis buffer composed of the solution described in *4.3.5* plus EDTA-free Halt™ Protease and Phosphatase inhibitor cocktail (Thermo Fisher Scientific), IGEPAL CA-630 (0,05%) as previously described [23]. Cell debris was removed by centrifugation at 10,000 × g for 15 min, and cytokine and growth factor levels were assessed in the supernatant. Different dilutions were obtained depending on the factor to quantify. The sample was left pure for IFN-γ (R&D Systems, Minneapolis, USA), diluted 1:5 for TGF-β1 (Boster Biological Technology, Pleasanton, USA), 1:20 for VEGF (R&D Systems), and 1:10 for IL-1β (R&D Systems). The concentration of each protein was then evaluated according to the specific manufacturer's instructions.

4.3.12. Statistics

All data are shown as mean ± standard error of the mean (SEM). Significance was assessed with a two-tailed ANOVA test performed with GraphPad Prism software (GraphPad, La Jolla, California, USA). P-values ≤ 0.05 were considered statistically significant. For experiments involving animals, the group size and statistical power were selected *a priori*, based on previous data [20], using an online sample size calculator (clincalc.com/stats/simplesize.aspx).

CRediT authorship contribution statement

Rosaria Volpini: Writing – review & editing, Writing – original draft, Validation, Supervision, Methodology, Conceptualization. **Catia Lambertucci:** Writing – original draft, Methodology, Investigation, Formal analysis, Conceptualization. **Luigia Ruo:** Investigation, Data curation. **Marcello Leopoldo:** Writing – review & editing, Writing – original draft, Supervision, Conceptualization. **Daniele Vitone:** Writing – original draft, Investigation. **Federica Fortuna:** Writing – original draft, Investigation, Data curation. **Enza Lacivita:** Writing – review & editing, Writing – original draft, Supervision, Methodology, Data curation, Conceptualization. **Beatrice Francucci:** Investigation. **Marianna Grignolo:** Writing – review & editing, Writing – original draft, Investigation, Formal analysis, Data curation. **Michela Buccioni:** Supervision, Methodology, Investigation, Conceptualization. **Elena Adinolfi:** Writing – review & editing, Writing – original draft, Validation, Supervision, Investigation, Funding acquisition, Data curation, Conceptualization. **Diego Dal Ben:** Writing – review & editing, Writing – original draft, Funding acquisition, Formal analysis, Conceptualization. **Ludovica Ricci:** Writing – review & editing, Writing – original draft, Investigation, Formal analysis, Conceptualization. **Gabriella Marucci:** Investigation, Data curation. **Andrea Spinaci:** Writing – original draft, Methodology, Investigation, Data curation. **Anna Pegoraro:** Writing – review & editing, Writing – original draft, Supervision, Investigation, Conceptualization.

Authors contribution

EA, RV, MG, AS, EL, L Ricci, AP conceived and designed the study, wrote and revised the manuscript. MG, AS, L Ricci AP, L Ruo, CL, DV, FF, MB, BF, GM performed the experiments, DDB performed molecular modeling analysis, MG, AS, L Ricci, AP, L Ruo, MB, BF, GM, CL, DDB, RV, EL, EA analyzed and interpreted the data. CL, DDB, ML, EL participated in experimental design. All authors reviewed and approved the final manuscript.

Ethics declarations

The animal study was reviewed and approved by the Organismo Preposto al Benessere Animale (OPBA, organism for Animal Wellbeing), the University of Ferrara, and the Italian Ministry of Health.

Funding

The research leading to these results has received funding from AIRC under IG 2019- ID. 22837 IG 2025-ID 31958 projects P.I. Adinolfi Elena, this work was also supported by the PurTher TRANSCAN3 project to EA; Programmi di Ricerca Scientifica di Rilevante Interesse Nazionale (PRIN 2022 5LKPYA to EA and DDB).

Declaration of Competing Interest

The authors declare the following financial interests/personal relationships which may be considered as potential competing interests: Elena Adinolfi reports financial support was provided by Italian Association for Cancer Research. Elena Adinolfi reports financial support was provided by ERA-NET Transcan 3. Elena Adinolfi reports financial support was provided by Italian Ministry of Research and University. Diego Dal Ben reports financial support was provided by Italian Ministry of Research and University. Elena Adinolfi reports a relationship with University of Ferrara that includes: employment, funding grants, non-financial support, and travel reimbursement. Marianna Grignolo reports a relationship with University of Ferrara that includes: employment and travel reimbursement. Andrea Spinaci reports a relationship with University of Camerino that includes: employment. Anna Pegoraro reports a relationship with University of Ferrara that includes: employment and travel reimbursement. Luigia Ruo reports a relationship with University of Ferrara that includes: employment and travel reimbursement. Catia Lambertucci reports a relationship with University of Camerino that includes: employment. Daniele Vitone reports a relationship with University of Bari that includes: employment. Marcello Leopoldo reports a relationship with University of Bari that includes: employment, funding grants, non-financial support, and travel reimbursement. Enza Lacivita reports a relationship with University of Bari that includes: employment, funding grants, non-financial support, and travel reimbursement. Federica Fortuna reports a relationship with Univeristy of Ferrara that includes: employment and travel reimbursement. Michela Buccioni reports a relationship with University of Camerino that includes: employment, funding grants, non-financial support, and travel reimbursement. Beatrice Francucci reports a relationship with Univeristy of Camerino that includes: employment. Gabriella Marucci reports a relationship with University of Camerino that includes: employment, funding grants, non-financial support, and travel reimbursement. Diego Dal Ben reports a relationship with University of Camerino that includes: employment, funding grants, non-financial support, and travel reimbursement. Rosaria Volpini reports a relationship with University of Camerino that includes: employment, funding grants, non-financial support, and travel reimbursement. The authors have no other copeting interest to disclose If there are other authors, they declare that they have no known competing financial interests or personal relationships that could have appeared to influence the work reported in this paper

Acknowledgments

The authors thank Dr. Simonetta Falzoni for fruitful discussion, Mrs. Marzia Scarletti and Dr. Federica Poletti for technical assistance, Prof. Massimo Bonora and Dr. Diego Chianese for help with cell membrane immunoblots. This article is based upon work from PRESTO COST Action CA21130, supported by COST (European Cooperation in Science and Technology) www.cost.eu; www.p2xcost.eu.

Data Availability

Data will be made available on request.

References

[1] F. Di Virgilio, G. Schmalzing, F. Markwardt, The Elusive P2X7 macropore, Trends Cell Biol. 28 (5) (2018) 392–404.
[2] R.A. North, P2X receptors, Philos. Trans. R. Soc. Lond. B Biol. Sci. 371 (1700) (2016).
[3] R.A. North, Molecular physiology of P2X receptors, Physiol. Rev. 82 (4) (2002) 1013–1067.
[4] A. Karasawa, T. Kawate, Structural basis for subtype-specific inhibition of the P2X7 receptor, Elife 5 (2016).
[5] G. Scarpellino, T. Genova, L. Munaron, Purinergic P2X7 receptor: a cation channel sensitive to tumor microenvironment, Recent Pat. Anticancer Drug Discov. 14 (1) (2019) 32–38.
[6] F. Di Virgilio, et al., Extracellular ATP and P2 purinergic signalling in the tumour microenvironment, Nat. Rev. Cancer (2018).
[7] E. Adinolfi, et al., The P2X7 receptor in oncogenesis and metastatic dissemination: new insights on vesicular release and adenosinergic crosstalk, Int. J. Mol. Sci. 24 (18) (2023).
[8] A. Pegoraro, et al., P2X7 variants in pathophysiology, Int. J. Mol. Sci. 25 (12) (2024).
[9] Y.T. Zou, et al., The impact of the P2X7 receptor on the tumor immune microenvironment and its effects on tumor progression, Biochem. Biophys. Res. Commun. 707 (2024) 149513.
[10] I.L.A. Rabelo, et al., Cancer metabostemness and metabolic reprogramming via P2X7 receptor, Cells 10 (7) (2021).
[11] E. Adinolfi, et al., Expression of P2X7 receptor increases in vivo tumor growth, Cancer Res. 72 (12) (2012) 2957–2969.
[12] F. Amoroso, et al., The P2X7 receptor is a key modulator of the PI3K/GSK3beta/VEGF signaling network: evidence in experimental neuroblastoma, Oncogene 34 (41) (2015) 5240–5251.
[13] R. Lara, et al., P2X7 in cancer: from molecular mechanisms to therapeutics, Front. Pharm. 11 (2020) 793.
[14] M. Demeules, et al., Evaluation of nanobody-based biologics targeting purinergic checkpoints in tumor models in vivo, Front. Immunol. 13 (2022) 1012534.
[15] B. Jelassi, et al., P2X(7) receptor activation enhances SK3 channels- and cystein cathepsin-dependent cancer cells invasiveness, Oncogene 30 (18) (2011) 2108–2122.
[16] B. Jelassi, et al., Anthraquinone emodin inhibits human cancer cell invasiveness by antagonizing P2X7 receptors, Carcinogenesis 34 (7) (2013) 1487–1496.
[17] F. Di Virgilio, et al., P2 receptors in cancer progression and metastatic spreading, Curr. Opin. Pharm. 29 (2016) 17–25.
[18] A. Pegoraro, et al., P2X7 promotes metastatic spreading and triggers release of miRNA-containing exosomes and microvesicles from melanoma cells, Cell Death Dis. 12 (12) (2021) 1088.
[19] W.J. Zhang, et al., P2X7 receptor promotes the growth and metastasis of gastric cancer by activating P13/AKT/GSK-3 beta signaling (experimental research), Int. J. Surg. 111 (6) (2025) 3752–3766.
[20] E. De Marchi, et al., A2A receptor contributes to tumor progression in P2X7 null mice, Front Cell Dev. Biol. 10 (2022) 876510.
[21] E. Orioli, et al., P2X7 receptor orchestrates multiple signalling pathways triggering inflammation, autophagy and metabolic/trophic responses, Curr. Med. Chem. 24 (21) (2017) 2261–2275.
[22] F. Di Virgilio, et al., Overview of the role of purinergic signaling and insights into its role in cancer therapy, Pharm. Ther. 262 (2024) 108700.
[23] A. Pegoraro, et al., P2X7 a new therapeutic target to block vesicle-dependent metastasis in colon carcinoma: role of the A2A/CD39/CD73 axis, Cell Death Dis. 16 (1) (2025) 587.
[24] F. Di Virgilio, et al., The P2X7 receptor in Infection and Inflammation, Immunity 47 (1) (2017) 15–31.
[25] M. Li, et al., The expression of P2X7 receptor on Th1, Th17, and regulatory T cells in patients with systemic lupus erythematosus or rheumatoid arthritis and its correlations with active disease, J. Immunol. 205 (7) (2020) 1752–1762.
[26] C. Xu, et al., Selective regulation of IFN-gamma and IL-4 co-producing unconventional T cells by purinergic signaling, J. Exp. Med. 221 (12) (2024).
[27] E. De Marchi, et al., The P2X7 receptor modulates immune cells infiltration, ectonucleotidases expression and extracellular ATP levels in the tumor microenvironment, Oncogene (2019).
[28] E. Adinolfi, et al., Role of the P2X7 receptor in tumor-associated inflammation, Curr. Opin. Pharm. 47 (2019) 59–64.
[29] F. Grassi, B. De Ponte Conti, The P2X7 Receptor in Tumor Immunity. Front. Cell Dev. Biol. 9 (2021) 694831.
[30] M. Zanoni, et al., Emerging roles of purinergic signaling in anticancer therapy resistance, Front. Cell Dev. Biol. 10 (2022) 1006384.
[31] C.E. Muller, V. Namasivayam, Agonists, antagonists, and modulators of P2X7 receptors, Methods Mol. Biol. 2510 (2022) 31–52.
[32] S.M. Gilbert, et al., A phase I clinical trial demonstrates that nfP2X7 -targeted antibodies provide a novel, safe and tolerable topical therapy for basal cell carcinoma, Br. J. Dermatol. 177 (1) (2017) 117–124.
[33] V. Bandara, et al., Engineered CAR-T cells targeting the non-functional P2X purinoceptor 7 (P2X7) receptor as a novel treatment for ovarian cancer, Clin. Transl. Immunol. 13 (5) (2024) e1512.
[34] I.G. El Idrissi, et al., Structure-activity relationships and therapeutic potential of purinergic P2X7 receptor antagonists, Curr. Med. Chem. 31 (11) (2024) 1361–1403.
[35] M. Murgia, et al., Oxidized ATP. An irreversible inhibitor of the macrophage purinergic P2Z receptor, J. Biol. Chem. 268 (11) (1993) 8199–8203.
[36] L.H. Jiang, et al., Brilliant blue G selectively blocks ATP-gated rat P2X(7) receptors, Mol. Pharm. 58 (1) (2000) 82–88.
[37] C.E. Gargett, J.S. Wiley, The isoquinoline derivative KN-62 a potent antagonist of the P2Z-receptor of human lymphocytes, Br. J. Pharm. 120 (8) (1997) 1483–1490.
[38] R.D. Beigi, et al., Oxidized ATP (oATP) attenuates proinflammatory signaling via P2 receptor-independent mechanisms, Br. J. Pharm. 140 (3) (2003) 507–519.
[39] D.L. Donnelly-Roberts, et al., Mammalian P2X7 receptor pharmacology: comparison of recombinant mouse, rat and human P2X7 receptors, Br. J. Pharm. 157 (7) (2009) 1203–1214.
[40] A. Brandao-Burch, et al., The P2X7 receptor is an important regulator of extracellular ATP Levels, Front Endocrinol. (Lausanne) 3 (2012) 41.
[41] M. Eggers, et al., Nanobodies as probes to investigate purinergic signaling, Biochem. Pharm. 187 (2021) 114394.
[42] W. Carroll, A. F, A. Perez-Medrano, S. PeddiP2X7 receptor antagonists and methods of use, Patent: US20070105842A12007.
[43] J.P. Kilburn, L.K. Rasmussen, M. Jessing, E.M. Eldemenky, B. Chen, Y. Jiang, 2014, Cyclic amines, Patent: US0107335A1: United States 2014.
[44] A.S. Florjancic, et al., synthesis and in vitro activity of 1-(2,3-dichlorophenyl)-N-(pyridin-3-ylmethyl)-1H-1,2,4-triazol-5-amine and 4-(2,3-dichlorophenyl)-N-(pyridin-3-ylmethyl)-4H-1,2,4-triazol-3-amine P2X7 antagonists, Bioorg. Med. Chem. Lett. 18 (6) (2008) 2089–2092.
[45] A. Surprenant, et al., The cytolytic P2Z receptor for extracellular ATP identified as a P2X receptor (P2X7), Science 272 (5262) (1996) 735–738.
[46] P. Honore, et al., A-740003 [N-(1-{[(cyanoimino)(5-quinolinylamino) methyl] amino}-2,2-dimethylpropyl)-2-(3,4-dimethoxyphenyl)acetamide], a novel and selective P2X7 receptor antagonist, dose-dependently reduces neuropathic pain in the rat, J. Pharm. Exp. Ther. 319 (3) (2006) 1376–1385.
[47] E. Adinolfi, et al., Basal activation of the P2X7 ATP receptor elevates mitochondrial calcium and potential, increases cellular ATP levels, and promotes serum-independent growth, Mol. Biol. Cell 16 (7) (2005) 3260–3272.
[48] E. Adinolfi, et al., Trophic activity of a naturally occurring truncated isoform of the P2X7 receptor, FASEB J. 24 (9) (2010) 3393–3404.
[49] A.C. Oken, et al., A polycyclic scaffold identified by structure-based drug design effectively inhibits the human P2X7 receptor, Nat. Commun. 16 (1) (2025) 8283.
[50] Molecular Operating Environment (MOE). 2025, C.C.G., Inc., 1255 University St., Suite 1600, Montreal, Quebec, Canada, H3B 3×3.
[51] A.C. Oken, et al., P2X(7) receptors exhibit at least three modes of allosteric antagonism, Sci. Adv. 10 (40) (2024) eado5084.
[52] R.S. Obach, et al., The prediction of human pharmacokinetic parameters from preclinical and in vitro metabolism data, J. Pharm. Exp. Ther. 283 (1) (1997) 46–58.
[53] L. Di, et al., Applications of high throughput microsomal stability assay in drug discovery, Comb. Chem. High. Throughput Screen 11 (6) (2008) 469–476.
[54] F. Di Virgilio, et al., structure, function and techniques of investigation of the P2X7 receptor (P2X7R) in mammalian cells, Methods Enzym. 629 (2019) 115–150.
[55] B. Szymczak, et al., Retinoic acid-induced alterations enhance eATP-mediated anticancer effects in glioma cells: implications for P2X7 receptor variants as key players, Biochim. Biophys. Acta Mol. Basis Dis. 1871 (3) (2025) 167611.
[56] E. Adinolfi, et al., Emerging roles of P2X receptors in cancer, Curr. Med. Chem. 22 (7) (2015) 878–890.
[57] F. Hattori, et al., Feasibility study of B16 melanoma therapy using oxidized ATP to target purinergic receptor P2X7, Eur. J. Pharm. 695 (1-3) (2012) 20–26.
[58] J.G. McLarnon, Roles of purinergic P2X7 receptor in glioma and microglia in brain tumors, Cancer Lett. 402 (2017) 93–99.
[59] M. Zanoni, et al., Irradiation causes senescence, ATP release, and P2X7 receptor isoform switch in glioblastoma, Cell Death Dis. 13 (1) (2022) 80.
[60] E. Adinolfi, et al., Accelerated tumor progression in mice lacking the ATP receptor P2X7, Cancer Res. 75 (4) (2015) 635–644.
[61] N. Murphy, M.A. Lynch, Activation of the P2X(7) receptor induces migration of glial cells by inducing cathepsin B degradation of tissue inhibitor of metalloproteinase 1, J. Neurochem. 123 (5) (2012) 761–770.
[62] B.J. Gu, J.S. Wiley, Rapid ATP-induced release of matrix metalloproteinase 9 is mediated by the P2X7 receptor, Blood 107 (12) (2006) 4946–4953.
[63] M. Wolosowicz, S. Prokopiuk, T.W. Kaminski, The complex role of matrix metalloproteinase-2 (MMP-2) in health and disease, Int. J. Mol. Sci. 25 (24) (2024).
[64] M. Catalano, L. O'Driscoll, Inhibiting extracellular vesicles formation and release: a review of EV inhibitors, J. Extra Vesicles 9 (1) (2020) 1703244.
[65] N. Irep, et al., Exosome inhibition improves response to first-line therapy in small cell lung cancer, J. Cell Mol. Med. 28 (4) (2024) e18138.
[66] E. De Marchi, et al., Detection of extracellular ATP in the tumor microenvironment, using the pmeLUC biosensor, Methods Mol. Biol. 2041 (2020) 183–195.
[67] B. Zhou, et al., Interferon-gamma signaling promotes melanoma progression and metastasis, Oncogene 42 (5) (2023) 351–363.
[68] D.V.F. Tauriello, E. Sancho, E. Batlle, Overcoming TGFbeta-mediated immune evasion in cancer, Nat. Rev. Cancer 22 (1) (2022) 25–44.
[69] H.C. Kolb, et al., Preclinical evaluation and nonhuman primate receptor occupancy study of (18)F-JNJ-64413739, a PET radioligand for P2X7 receptors, J. Nucl. Med. 60 (8) (2019) 1154–1159.
[70] M.J. Morytko, et al., Synthesis and in vitro activity of N′-cyano-4-(2-phenylacetyl)-N-o-tolylpiperazine-1-carboximidamide P2X7 antagonists, Bioorg. Med. Chem. Lett. 18 (6) (2008) 2093–2096.

[71] A.L. Giuliani, et al., Trophic activity of human P2X7 receptor isoforms A and B in osteosarcoma, PLoS One 9 (9) (2014) e107224.
[72] E. De Marchi, A. Pegoraro, E. Adinolfi, Administration of P2X7 receptor blockers in oncological experimental models, Methods Mol. Biol. 2510 (2022) 303–314.
[73] P. Workman, et al., Guidelines for the welfare and use of animals in cancer research, Br. J. Cancer 102 (11) (2010) 1555–1577.